

Recent results from deuterium experiments on the large helical device and their contribution to fusion reactor development

journal or publication title	Nuclear Fusion
volume	62
number	4
page range	042019
year	2022-02-14
NAIS	12976
URL	http://hdl.handle.net/10655/00013069

doi: 10.1088/1741-4326/ac3cda



PAPER • OPEN ACCESS

Recent results from deuterium experiments on the large helical device and their contribution to fusion reactor development

To cite this article: Masaki Osakabe *et al* 2022 *Nucl. Fusion* **62** 042019

View the [article online](#) for updates and enhancements.

You may also like

- [Enhancement of helium exhaust by resonant magnetic perturbation fields at LHD and TEXTOR](#)
O. Schmitz, K. Ida, M. Kobayashi *et al.*
- [Edge impurity transport study in the stochastic layer of LHD and the scrape-off layer of HL-2A](#)
M. Kobayashi, S. Morita, C.F. Dong *et al.*
- [A review of impurity transport characteristics in the LHD](#)
Shigeru Sudo

Recent results from deuterium experiments on the large helical device and their contribution to fusion reactor development

Masaki Osakabe^{1,2,*}, Hiromi Takahashi^{1,2}, Hiroshi Yamada³,
Kenji Tanaka^{1,4}, Tatsuya Kobayashi¹, Katsumi Ida^{1,2},
Satoshi Ohdachi^{1,3}, Jacobo Varela⁵, Kunihiro Ogawa^{1,2},
Masahiro Kobayashi^{1,2}, Katsuyoshi Tsumori^{1,2},
Katsunori Ikeda¹, Suguru Masuzaki^{1,2}, Masahiro Tanaka¹,
Motoki Nakata¹, Sadayoshi Murakami⁶, Shigeru Inagaki⁴,
Kiyofumi Mukai^{1,2}, Mizuki Sakamoto⁷, Kazunobu Nagasaki⁸,
Yasuhiro Suzuki^{1,2,9}, Mitsutaka Isobe^{1,2}, Tomohiro Morisaki^{1,2}
and the LHD Experiment Group

¹ National Institute for Fusion Science, National Institutes of Natural Sciences, Toki, Gifu 509-5292 Japan

² The Graduate University for Advanced Studies, SOKENDAI, Toki, Gifu 509-5292, Japan

³ The University of Tokyo, Kashiwa, Chiba 277-8568, Japan

⁴ Kyushu University, Kasuga, Fukuoka 816-8580, Japan

⁵ Universidad Carlos III de Madrid, 28911 Leganes, Madrid, Spain

⁶ Kyoto University, Kyoto, Kyoto 615-8540, Japan

⁷ University of Tsukuba, Ibaraki 305-8577, Japan

⁸ Kyoto University, Uji, Kyoto 611-0011, Japan

E-mail: osakabe.masaki@nifs.ac.jp

Received 8 October 2021, revised 8 November 2021

Accepted for publication 24 November 2021

Published 14 February 2022




Abstract

In recent deuterium experiments on the large helical device (LHD), we succeeded in expanding the temperature domain to higher regions for both electron and ion temperatures. Suppression of the energetic particle driven resistive interchange mode (EIC) by a moderate electron temperature increase is a key technique to extend the high temperature domain of LHD plasmas. We found a clear isotope effect in the formation of the internal transport barrier in high temperature plasmas. A new technique to measure the hydrogen isotope fraction was developed in the LHD in order to investigate the behavior of the isotope mixing state. The technique revealed that the non-mixing and the mixing states of hydrogen isotopes can be realized in plasmas. In deuterium plasmas, we also succeeded in simultaneously realizing the formation of the edge transport barrier (ETB) and the divertor detachment. It is found that resonant magnetic perturbation plays an important role in the simultaneous formation of the ETB and the detachment. Contributions to fusion reactor development from the engineering point of view, i.e. negative-ion based neutral beam injector research and the mass balance study of tritium, are also discussed.

* Author to whom any correspondence should be addressed.

⁹ Present address: Hiroshima University, Higashi-Hiroshima, Hiroshima 739-8527, Japan

 Original content from this work may be used under the terms of the [Creative Commons Attribution 4.0 licence](https://creativecommons.org/licenses/by/4.0/). Any further distribution of this work must maintain attribution to the author(s) and the title of the work, journal citation and DOI.

Keywords: LHD, stellarator, isotope effect, deuterium experiment, energetic particle confinement, RMP induced H-mode, tritium mass balance

(Some figures may appear in colour only in the online journal)

1. Introduction

Deuterium experiments were conducted on the large helical device (LHD) since March 2017 [1–3]. The objectives of these experiments are to (1) realize high performance plasmas that can foresee reactor relevant plasmas in the helical system using the benefit of isotope effects in plasma confinement and an upgraded heating device, (2) explore the physics related to the isotope effect in toroidal plasmas, (3) investigate the confinement property of energetic particles (EPs) in helical plasmas and (4) extend the plasma–material interaction, especially the retention of hydrogen isotopes inside the machine, using the steady state operability of the LHD. The experiments will demonstrate the scientific feasibility of a helical-type fusion reactor and will provide important information in developing operation scenarios and a comprehensive understanding of the physics for future reactor plasmas.

In the first campaign of the deuterium experiment in 2017, an ion temperature (T_i) of 10 keV was achieved for the first time in helical devices [3]. The achieved electron temperature (T_e) was ~ 4 keV for high ion temperature plasmas. In a future fusion reactor, high temperature plasmas will be mainly sustained by energetic alpha particles, produced by a deuterium–tritium (D–T) fusion reaction. Because the initial energy of the alpha particle is much higher than the critical energy ($E_c \approx 37.2T_e$), the heating power from alpha particles to bulk ions becomes comparable to that of bulk electrons, and electron heating is dominant in such a fusion sustained plasma. Thus, it is expected that the T_e is larger than or at least comparable to the T_i in fusion sustained plasmas. Conversely, it is pointed out that the confinement property of such an electron-heat dominant plasma might be degraded because turbulence transport becomes significant when the T_e/T_i ratio becomes high [4, 5]. Therefore, exploring the high electron temperature region of high ion temperature plasmas and investigating their confinement properties are important.

The isotope effect is a long underlying mystery in plasma physics because most experimental observations in tokamak plasmas show favorable effects from the ion mass on the energy confinement time (τ_E) while the theoretical prediction based on the gyro-Bohm model shows an unfavorable effect, i.e. $\tau_E \propto M^{-1/2}$. The isotope effect of L-mode confinement plasmas was investigated by comparing dimensionally similar hydrogen and deuterium plasmas in the LHD and showed the existence of a mass dependent factor in the empirical scaling law of confinement time, in addition to the gyro-Bohm dependence [6]. The comparison has been extended recently to mixture plasmas to achieve a more general understanding of the τ_E . The isotope effect on plasmas is also evaluated with

the internal transport barrier (ITB) by defining an ITB intensity [7]. Particle behaviors of hydrogen isotopes in their mixture plasmas are also important because the fusion output of future reactors is dominated by the ratio of D and T ions in plasmas. A new technique based on charge exchange spectroscopy (CXS) to investigate the hydrogen isotope fraction was developed to investigate the behavior of hydrogen isotopes in their mixture plasmas [8].

Investigation of the EP confinement property in helical plasmas is also an important issue in LHD deuterium experiments. Because a neutron produced by the deuterium–deuterium (D–D) fusion reaction exhibits a larger cross section as the relative energy between reactant ions increases, the neutron diagnostic can be used as a good tool to evaluate the confinement properties of EPs. In the first year of the deuterium experiment, we successfully demonstrated that the LHD has good EP confinement properties which are comparable to tokamak devices with a similar size in the poloidal cross section, such as the KSTAR using a triton burn-up experiment [9]. Through the deuterium experiment, we are also constructing an EP-confinement database of helical system for quiescent plasmas using an NB-blip experiment and have revealed its confinement property through a comparison to a numerical simulation code, i.e. GNET [10]. The interactions between EPs and EP-driven instabilities are of our great interest. A significant loss of up to 60% of EPs, produced by NB injection, by the influence of the EP driven resistive interchange mode (EIC), was reported [11]. Since the loss of EPs by the EIC is a significant obstacle in extending high temperature plasmas in the LHD, a method to control the EIC [12] and the influence of the EIC on EPs were investigated [11, 13].

The realization of both divertor heat load mitigation and good core confinement properties is an important issue in developing future reactor scenarios. The resonant magnetic perturbation (RMP) is utilized to stabilize the detachment [14, 15]. It was found that the expansion of the low temperature region below 20 eV, enables enhanced radiation power that almost reaches 60% of the input heating power. An edge transport barrier (ETB) was formed at the confinement boundary at the onset of detachment. Further improvement in confinement, i.e. an RMP induced H-mode, was also found after the onset [16].

The contribution to fusion reactor development from an engineering point of view is also an important aspect of the LHD deuterium experiment. Especially, the contribution to the development of negative-ion based neutral beam injectors (N-NBIs) is very important for the ITER and/or future fusion reactor development because the LHD is the only machine which has demonstrated the reliable operation of multiple N-NBIs for

more than twenty years and also shows that the requirements of the ITER-NBI in a beam current, beam divergent angle, and co-extracted electron fraction can be simultaneously fulfilled in real plasma experiments. This fact strongly encourages the use of N-NBI in the ITER. The tritium mass balance study is also an important contribution of the LHD deuterium experiment, because the LHD is the only toroidal plasma confining device which can monitor the tritium amount contained in the whole vacuum exhaust, not only from the torus but also the peripheral devices which connect to the torus, except the JET where tritium can be used as a fueling gas. Investigation of tritium distribution in the torus is also important to examine EP behavior in the device, because the initial energy of tritium by the deuterium–deuterium (D–D) fusion reaction is very high, i.e. ~ 1 MeV.

In this paper, recent research activities on the LHD are reported. The extension of the temperature domain of LHD plasmas is reported in section 2. The exploration of the physics related to hydrogen isotopes is reported in section 3. Control of the EIC and the effect of the EIC on EP transport is discussed in section 4. Realization of both divertor heat load mitigation and good core confinement properties with an RMP induced H-mode are shown in section 5. In section 6, contributions to fusion reactor development are shown from the engineering point of view, where the research and development activities for N-NBIs and tritium mass balance studies are discussed. Section 7 is the summary.

2. Extension of high temperature domain of LHD plasmas

Recent activities in extending the high temperature domain of LHD plasmas are summarized in figure 1(a). As shown in this figure, the achieved high T_i domain was successfully expanded to the high T_e region in the deuterium experiment. The expansion of high T_i plasmas to the high T_e region becomes possible mainly due to the suppression of the EIC, which causes significant loss of EPs, by an increase of T_e with the superposition of electron cyclotron heating (ECH) with high- T_i plasmas [17]. Presently, we successfully achieved the $T_i = 10$ keV and $T_e = 6.6$ keV with mitigation of the EIC by ECH. The main mechanism of EIC mitigation by ECH is reduction of resistivity, which leads to narrowing the width of the EIC mode structure [18]. The detail of the EIC mitigation mechanisms is discussed in section 4.1 and can also be found in [18, 19]. Conversely, if the increase in T_e by ECH is significant, the thermal ion confinement property degrades with the increase of the T_e/T_i ratio [4, 5, 17]. Figure 1(b) shows the dependence of the normalized scale length of T_i on the T_e/T_i ratio at a normalized minor radius (r_{eff}/a_{99}) of 0.17. Here, r_{eff} is the effective minor radius defined as the radius of the equivalent simple torus which encloses the same volume as the toroidal flux of interest and a_{99} is the effective minor radius which encloses 99% of the total electron pressure [20]. This figure indicates that the existence of a threshold value in the T_e/T_i ratio at ~ 0.75 where the thermal ion confinement property is degraded and that the flattening of the T_i -profile occurs above the threshold. These results show that the control of T_e at

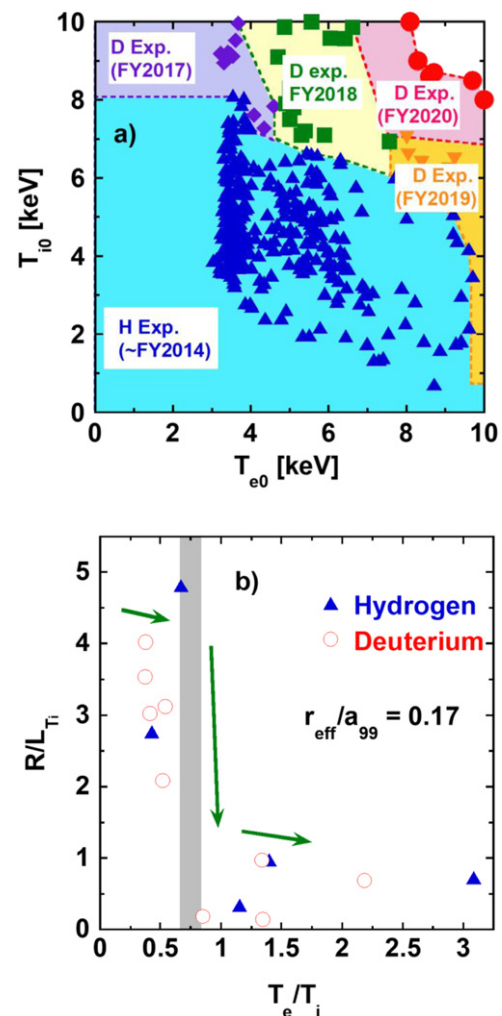


Figure 1. (a) Temperature domain achieved in LHD. (b) Dependence of normalized scale length of T_i on T_e/T_i at normalized minor radius of $r_{\text{eff}}/a_{99} = 0.17$. (Reproduced with permission from [17].)

a moderately high value, i.e. $T_e = \sim 0.75T_i$, is important in achieving high- T_i plasmas to simultaneously mitigate the EIC and avoid confinement degradation of thermal ions [5, 17].

Figure 2 shows the radial profile of T_e , T_i and thermal diffusivities for electrons (χ_e) and ions (χ_i) for high temperature discharges with and without on-axis ECH superposition [17]. Applying the ECH superposition, the T_e gradient increased at the center region and the reduction of χ_e , especially in the region $r_{\text{eff}}/a_{99} < \sim 0.4$ due to electron ITB formation, was observed. For the ion thermal confinement, the χ_i reflects the tendency of the T_i gradient and χ_i with the ECH case was smaller than that without the ECH case, especially in the region around $r_{\text{eff}}/a_{99} = 0.6$ – 0.8 . Here, we have to note that the EP losses by the EICs were not included in the power balance analysis because an adequate simple EP loss model, which can be used for the analysis, was not constructed, yet. Thus, the ion-heating power was overestimated in the power balance analysis when the EIC was excited. This leads to an overestimation of χ_i when the EIC is excited. The EIC occurs as a result of interaction between helically trapped EPs and the resistive interchange (RIC) mode at $iota = 1$ surface, which usually locates

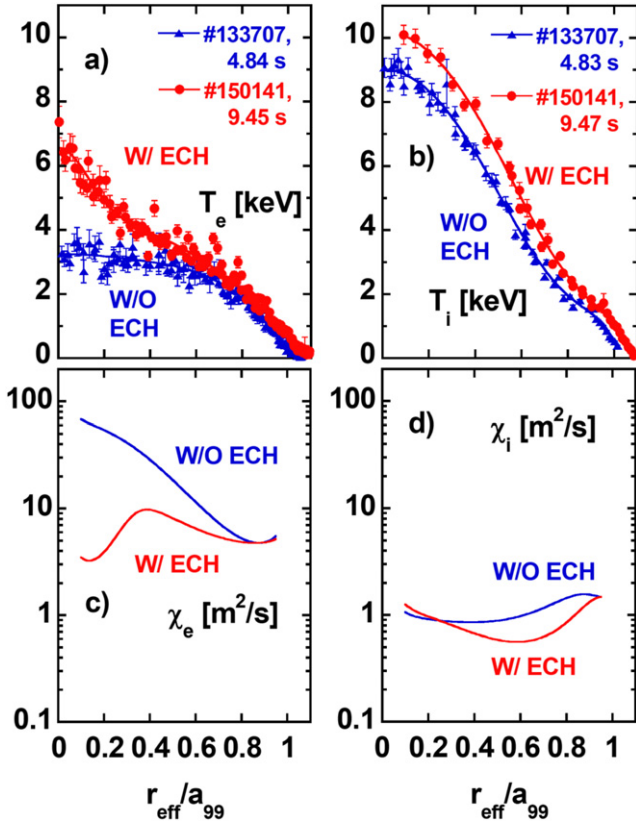


Figure 2. Radial profiles of (a) T_e , (b) T_i , (c) χ_e , and (d) χ_i without and with on-axis ECH superposition of 1.8 MW. (Reproduced with permission from [17].)

near $r_{\text{eff}}/a_{99} \sim 0.9$. It was found that the peak of EIC mode structure locates slightly inward to the peak location of the RIC and is at $r_{\text{eff}}/a_{99} \sim 0.8$ [21]. Thus, the decrement of actual ion heating power around $r_{\text{eff}}/a_{99} \sim 0.8$ is expected by the influence of the EIC. This interpretation is more or less consistent with the increase of χ_i without an ECH superposed case, where the EICs are not mitigated, as shown in figure 2(d). A simple EP loss model construction for power balance analysis is now under investigation based on the analysis shown in reference [8]. This model will validate the interpretation for χ_i overestimation by the EP losses by the influence of the EICs.

3. Isotope effect and phenomena related to hydrogen isotopes

3.1. Investigation of the isotope effect in L-mode plasmas (including ion species mixture plasmas)

As mentioned in the previous section, the isotope effect on τ_E of L-mode plasmas was investigated by comparing dimensionally similar plasmas of H and D ions [6, 22, 23]. In future fusion burning plasmas, D and T ions will co-exist. Thus, extending the understanding to mixture plasmas of hydrogen isotopes is important. A comparison of H, D and H/D mixture plasmas heated by the NBI at the configuration of $R_{\text{ax}} = 3.6$ m, which is the standard configuration of the LHD, was performed for dimensionally similar plasmas [23]. Here,

dimensionally similar means that the dimensionless parameters, which are normalized Larmor radius (ρ^*), normalized collisionality (ν^*) and normalized pressure (β), are kept at the same value. In order to keep ρ^* , ν^* and β the same value, the magnetic field strength (B), density (n), and temperature (T) must scale as $B \propto M^{3/4}$, $n \propto M$, and $T \propto M^{1/2}$, respectively, where M is a mass number [6, 22–25]. For mixture plasmas, the effective mass (M_{eff}) is adopted as M . The main heating scenario of these experiments is electron-heating by high-energy tangential N-NBI because the plasma initiation at non-ECH-resonant magnetic field strength (1.64 T) is only possible by hydrogen tangential N-NBI on the LHD [2, 26]. Figure 3 shows typical profiles of dimensionally similar experiments for hydrogen and deuterium plasmas. As shown in this figure, the normalized T_e , T_i and n_e profiles of hydrogen and deuterium plasmas are amazingly similar to each other. As a result, evaluated ρ^* , ν^* and β profiles for hydrogen and deuterium plasmas become almost identical. Figure 4 shows the comparison of τ_E in the experiment [23]. Here, stored thermal energy was evaluated by the measured temperature and density profile. The dilution of ions due to major impurities of helium and carbon was also considered. An empirical scaling law was achieved as

$$\tau_E^{\text{R360NBI}} \propto M^{-0.07 \pm 0.01} B^{0.85} \bar{n}_e^{0.73 \pm 0.01} P_{\text{abs}}^{-0.081 \pm 0.01}, \quad (1)$$

where the effective mass (M_{eff}) including the multi-ion effect was used as M [23].

Here, an almost negligible mass dependence was identified and contradictory to gyro-Bohm scaling, which exhibits a $M^{-0.2}$ dependence in engineering parameter scaling [27]. When τ_E normalized by ion gyrofrequency (Ω_i) is assumed to be expressed by 4 dimensionless parameters (M , ρ^* , ν^* and β), this scaling law can be rephrased as [23]

$$\tau_E^{\text{R360NBI}} \Omega_i \propto M^{0.94} \rho^{*-3.02} \nu^{*0.15} \beta^{-0.23}. \quad (2)$$

This expression exhibits a clear dependence on M , in addition to the gyro-Bohm dependence of $\tau_E \Omega_i \propto M^0 \rho^{*-3}$ [6, 23, 28]. The equation (2) is similar to the expression provided in the previous work [6], although the exponents of ν^* and β are slightly different.

In empirical scaling laws for tokamak-devices, mass dependence is also considered. For example, the favorable mass dependence of $M^{0.20}$ and $M^{0.19}$ is shown both for the ITER L-mode (ITER97-L) scaling and the ITER ELMy H-mode (IPB98(y,2)) scaling, with engineering variables like equation (1) [29, 30]. The physical expression for these two scalings are [30];

$$\begin{aligned} \tau_{E,\text{th}}^{\text{ITER97-L}} / \tau_B &\propto \rho^{*0.15} \beta^{-1.41} \nu^{*0.19} \\ &\times M^{0.67} q^{-3.74} \varepsilon^{-0.09} \kappa^{3.22}, \quad \text{and} \end{aligned} \quad (3)$$

$$\begin{aligned} \tau_E^{\text{IPB98(y,2)}} / \tau_B &\propto \rho^{*-0.70} \beta^{-0.90} \nu^{*-0.01} \\ &\times M^{0.96} q^{-3.0} \varepsilon^{0.73} \kappa^{2.3}, \end{aligned} \quad (4)$$

respectively. Here, τ_B is Bohm time, q is the safety factor, ε is the inverse aspect ratio, and κ is the elongation/ellipticity. The

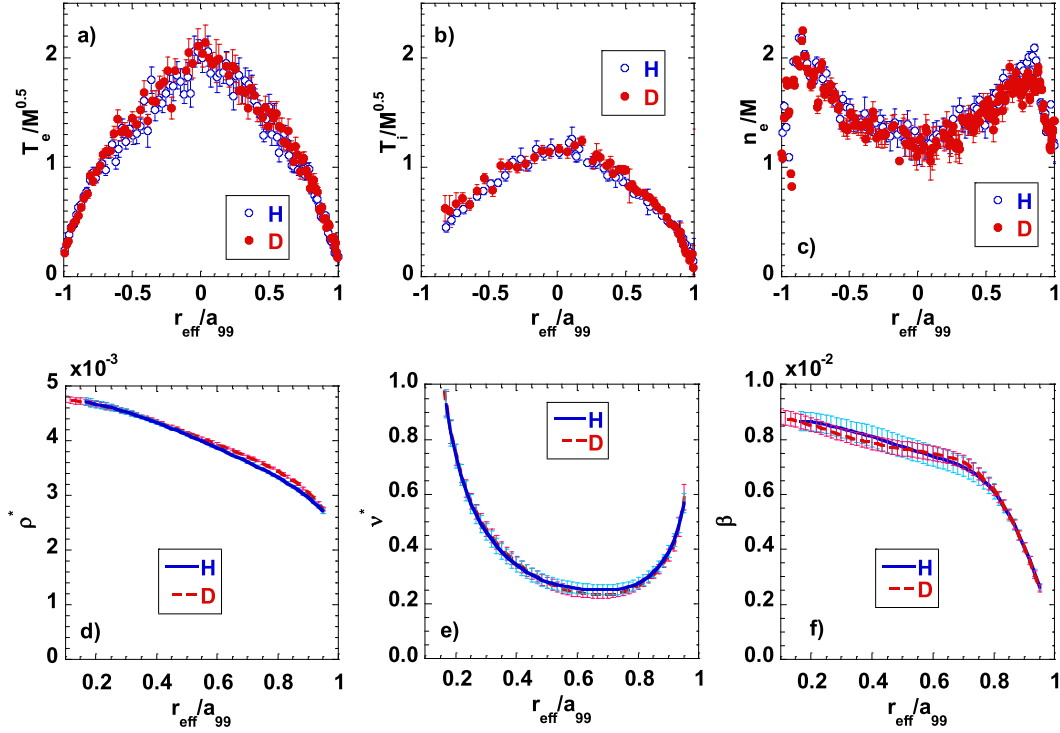


Figure 3. Profiles of dimensionally similar hydrogen and deuterium plasmas. (a) Normalized electron temperature, (b) ion temperature, and (c) electron density profiles shown by blue open circles for hydrogen and red closed circles for deuterium. Negative and positive sign in r_{eff}/a_{99} indicate inboard and outboard side location. Evaluated (d) ρ^* , (e) ν^* , and (f) local β profiles also shown by blue solid lines for hydrogen and red dashed lines for deuterium. Reprinted figure with permission from [6], Copyright (2019) by the American Physical Society.

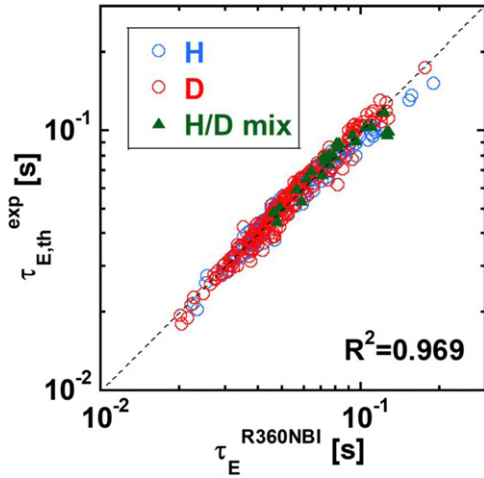


Figure 4. Comparison of energy confinement in experiment with empirical scaling law. (Reproduced with permission from [23].)

τ_B is defined as $\tau_B \equiv a^2 B/T$ using the minor radius (a), magnetic field strength (B), and temperature (T) [30]. Considering the fact that τ_B can be written as $\tau_B = 1/\Omega_i \rho^{*2}$ for hydrogen isotopes, equations (3) and (4) become;

$$\tau_{E,\text{th}}^{\text{ITER97-L}} \Omega_i \propto \rho^{*-1.85} \beta^{-1.41} \nu^{*0.19} \times M^{0.67} q^{-3.74} \epsilon^{-0.09} \kappa^{3.22}, \text{ and} \quad (5)$$

$$\tau_E^{\text{IPB98(y,2)}} \Omega_i \propto \rho^{*-2.70} \beta^{-0.90} \nu^{*-0.01} M^{0.96} q^{-3.0} \epsilon^{0.73} \kappa^{2.3}. \quad (6)$$

Comparing these equations to equation (2), it was found that the M and ρ^* dependences of the LHD L-mode are closer to those of the ELMy H-mode scaling in tokamaks although the confinement property of H-mode plasmas is originated from the ETB formation at the pedestal region, while the formation of ETB is not clear in LHD L-mode plasmas.

Thermal diffusivity in dimensionally similar plasmas has also been compared to clarify the character of the isotope effect. Figure 4 shows the comparison of thermal transport at a two thirds minor radius in dimensionally similar H and D plasmas [23]. Considering the fact that the global energy confinement time is roughly expressed by the square of the minor radius (a) and the reciprocal of thermal diffusivity (χ), i.e. $\tau_E \sim a^2/\chi$, and the mass dependence of equation (2) can be approximated by $\tau_E \Omega_i \propto M^1$, the normalized thermal diffusivity (χ/Ω_i) can be expressed as $\chi/\Omega_i \propto M^{-1}$. Thus, the ratio of normalized thermal diffusivity can be given by [22, 23];

$$\frac{\chi^D/\Omega_D}{\chi^H/\Omega_H} \cong \frac{M_H}{M_D} = 0.5, \quad (7)$$

and

$$(\chi^H/\Omega_H) = 2 (\chi^D/\Omega_D). \quad (8)$$

As shown in figure 5(a), the χ_e/Ω_i of hydrogen plasmas stayed almost twice as large as those of deuterium plasmas. This is consistent with equation (8). Conversely, the tendency of χ_i/Ω_i is different. As shown in figure 5(b), the χ_i/Ω_i of

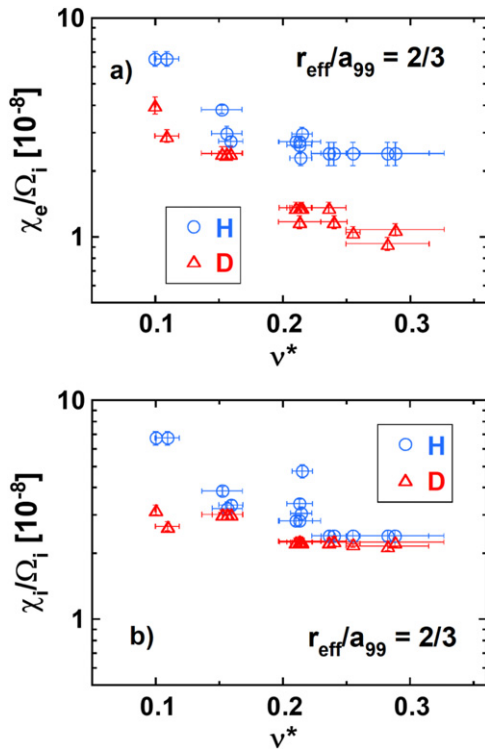


Figure 5. Comparison of (a) electron thermal diffusivity and (b) ion thermal diffusivity for dimensionally similar H and D plasmas (Reproduced with permission from [23]).

hydrogen plasmas are almost twice as large as those of deuterium plasmas at the low collisionality region. As the collisionality increases, the χ_i/Ω_i of both hydrogen and deuterium plasmas decreases and the difference between hydrogen and deuterium becomes almost none. The mechanism of this different tendency in ion thermal diffusivities at the high collisionality region is not clear yet. It must be noted that this discrepancy of χ_i/Ω_i from equation (8) at high collisionality will not affect the linear dependence of M in $\tau_E\Omega_i$ scaling, because the contribution of the ion confinement channel to the global confinement property is small under the electron heating dominant condition by energetic N-NBI [22, 23].

In figures 6(a) and (b), the normalized density fluctuation and density profiles are shown for a typical dimensionally similar pair of H and D plasmas at $\nu^* \approx 0.2$, respectively [22]. Here, density fluctuations are measured by a phase contrast imaging (PCI) diagnostic [31] and are normalized by the electron density of figure 6(b). The electron densities are evaluated by the Arbel inversion technique, using line integrated electron densities, measured by a far-infrared interferometer diagnostic, which locates next to the PCI diagnostic [32]. As shown in figure 6(a), the relative amplitude of hydrogen is larger than that of deuterium in the region between $r_{\text{eff}}/a_{99} = 0.5$ and 0.8. The k -spectra normalized by the ion Larmor radius (ρ_i) are also shown in figure 6(c) where the density fluctuation data between $r_{\text{eff}}/a_{99} = 0.5$ and 0.8 were used. The peak positions of the wave number spectra are almost same at $k\rho_i \approx 0.7$ and the peak amplitude is smaller for deuterium than for hydrogen. Coinciding reduction of density fluctuation and thermal

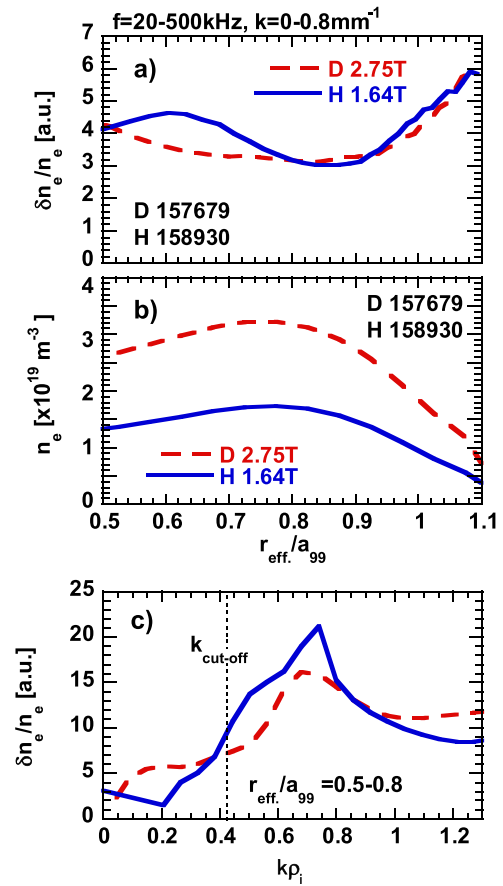


Figure 6. (a) Normalized electron density fluctuation profiles and (b) electron density profiles shown. Electron density profile evaluated by Arbel inversion technique using line integrated electron density measurements by FIR interferometers. Electron density fluctuation measured by PCI diagnostic and normalized by electron densities. (b) Wave number spectra for electron density fluctuation between $r = 0.5-0.8$. ((a) and (c) Reproduced from [22]. © IOP Publishing Ltd. CC BY 4.0.)

transport has been observed [22]. Further analysis based on gyrokinetic Vlasov (GKV) simulation [4] is ongoing to investigate the mechanism of the reduced transport and its relation with density fluctuation.

3.2. Isotope effect for plasmas with an ITB

In the high T_i plasmas on the LHD, the formation of an ITB is observed. To qualitatively investigate the isotope effect for plasmas with an ITB, we defined an ITB intensity;

$$(\text{ITB intensity}) \equiv \frac{\int n_i T_i dV}{\int n_i T_{i,L}^{\text{ref}} dV}, \quad (9)$$

where $T_{i,L}^{\text{ref}}$ is a reference ion temperature for L-mode plasmas [7, 33, 34]. The analysis was applied for plasmas of magnetic axis configurations of $R_{\text{ax}} = 3.55$ m, 3.58 m, and 3.6 m [33, 34], where high T_i plasmas scenario development was often performed because the neoclassical transport of LHD plasmas were predicted to be better at these inwardly shifted magnetic configurations, i.e. configurations of $R_{\text{ax}} < 3.75$ m. The configuration of $R_{\text{ax}} = 3.53$ m is called a neoclassical

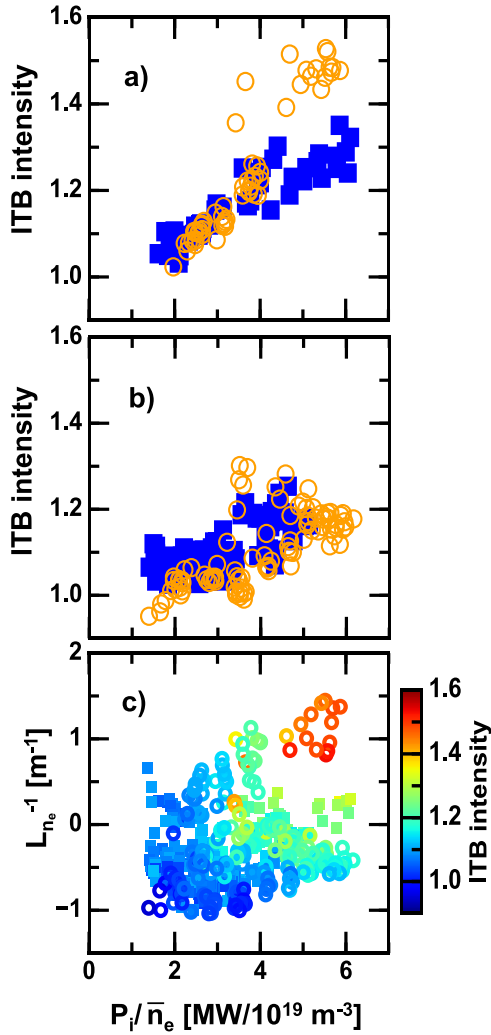


Figure 7. (a) Dependence of ITB intensity on P_i/\bar{n}_e for the magnetic-axis configuration of $R_{ax} = 3.55$ m and (b) for magnetic-axis configuration of $R_{ax} = 3.6$ m. Open circles and closed squares represent data from deuterium and hydrogen discharges, respectively. (c) ITB intensity distribution on P_i/\bar{n}_e and $L_{n_e}^{-1}$ for magnetic-axis configurations of $R_{ax} = 3.55$ m, 3.58 m and 3.6 m. Open circles and closed square represent data from deuterium and hydrogen discharges, respectively. Colors of symbols indicate ITB intensities. (Reproduced from [35]. © 2021 IAEA. CC BY 4.0.)

optimized configuration [35], but it was difficult to perform an experiment recently, due to the interference of EPs with the inboard side of the LHD-VV with the increased heating power of LHD-NBI and the $R_{ax} = 3.55$ m is the minimum major radius of the magnetic configuration with high-power NBI operation.

Figure 7(a) shows the dependence of the ITB intensity on the ion heating power density for a magnetic-axis configuration of $R_{ax} = 3.55$ m, where ion heating power is normalized by the line averaged electron density. A similar figure for a magnetic-axis configuration of $R_{ax} = 3.6$ m is also shown in figure 7(b). As shown in figures 7(a) and (b), the ITB intensity becomes larger as the ion heating power density increases. For a magnetic-axis configuration of $R_{ax} = 3.55$ m, the intensity is larger in deuterium than in hydrogen, when the ion

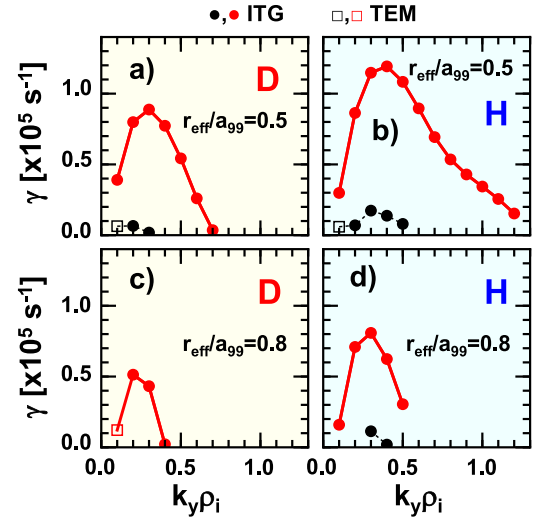


Figure 8. Turbulence linear growth rate calculated by GKV simulation for ITB and L-mode plasmas at $R_{ax} = 3.55$ m configuration. Simulation performed for D-plasmas (left column) and H-plasmas (right column), and at $r_{eff}/a_{99} = 0.5$ (top row) and 0.8 (bottom row). Red solid lines with symbols and black dashed lines with symbols indicate results for ITB plasmas and L-mode plasmas, respectively. Closed circles for ITG and open squares for TEM. (Reproduced from [35]. © 2021 IAEA. CC BY 4.0.)

heating power density is greater than 4 MW/10¹⁹ m⁻³. This indicates the existence of an isotope effect in plasmas with an ITB. Principal component analysis (PCA) was performed in the dimensional space of $(P_i/\bar{n}_e, G_{1,0}, L_{n_e}^{-1}, n_c, L_{n_c}^{-1})$, where n_e is the electron density, and n_c is the carbon density, evaluated by CXS. The L indicates the gradient scale length for each density profile at $r_{eff}/a_{99} = 0.6$ [33, 35] and is defined as;

$$L_\alpha^{-1} \equiv -\frac{1}{\alpha} \frac{\partial \alpha}{\partial r_{eff}}, \quad (10)$$

for a certain parameter α . These five parameters were chosen according to empirical experimental knowledge [3, 36–38] and theoretical predictions [4, 39, 40], where their impact of them on the micro-scale turbulence growth rate is pointed out. PCA determines the orthogonal principal component coordinates P_j , where ‘j’ is an index of natural numbers up to 5, in such a way the data variance is maximized, and data are regarded as points in the five dimensional space $(P_i/\bar{n}_e, G_{1,0}, L_{n_e}^{-1}, n_c, L_{n_c}^{-1})$ [34]. Here, direct impacts of the magnetic axis position and the plasma ion species are assumed to be less dominant, and their effect on the ITB strength through these plasma parameters is considered.

By the PCA, it was found that $L_{n_e}^{-1}$ and P_i/\bar{n}_e are important parameters for describing the dataset. In figure 7(c), all of the data points from magnetic-axis configurations of $R_{ax} = 3.55$ m, 3.58 m, and 3.6 m are plotted. As shown in this figure, the ITB intensity is large when $L_{n_e}^{-1}$ and P_i/\bar{n}_e are large, regardless of the difference of magnetic-axis configuration. This fact supports the hypothesis that the magnetic-axis configuration and the ion-species affect the ITB formation through plasma parameters [34]. The mechanism how these two quantities, i.e. $L_{n_e}^{-1}$ and P_i/\bar{n}_e , affect the formation of the ITB is not clear at present.

Table 1. List of discharges, where GKV simulations were performed, and their plasma parameters and ITB intensities [27].

Shot numbers	141209	141215	142541	142534
Fuel gas	D	D	H	H
\bar{n}_e ($\times 10^{19} \text{ m}^{-3}$)	1.25	3.69	1.11	3.77
$T_i(0)$ (keV)	5.5	2.4	3.2	2.4
$T_e(0)$ (keV)	2.9	2.7	3.5	3.2
ITB intensity	1.48	1.02	1.35	1.05
State	ITB	L-mode	ITB	L-mode

To explore the physics underlying the ITB formation, a series of GKV simulations was performed for an ITB D-plasma (#141209), an L-mode D-plasma (#141215), an ITB H-plasma (#142541), and an L-mode H-plasma (#142534) at $r_{\text{eff}}/a_{99} = 0.5$ and 0.8 , which correspond to the inside and the outside of the ITB foot point, respectively [32]. The results are shown in figure 8. As shown in figure 8, the ion temperature gradient mode (ITG) driven turbulence is unstable in most cases, and linear growth rates for ITB plasmas are one order larger than those for L-mode plasmas. In the case of L-mode D-plasma at $r_{\text{eff}}/a_{99} = 0.8$, the turbulence is found to be stable. The linear growth rates at the inner side of the ITB foot point ($r_{\text{eff}}/a_{99} = 0.5$) tend to be larger than those at outer side of the point ($r_{\text{eff}}/a_{99} = 0.8$) in both H and D ITB plasmas. This tendency is due to the large ITG which is formed inside the ITB. The relatively large linear growth rate in the H plasmas is qualitatively consistent with its weak ITB formation. The linear growth rate of turbulence is significantly smaller in the L-mode plasmas, although the input power, which corresponds to the total heat flux, is similar and the density differs only by a factor to the ITB plasmas as shown in table 1. Therefore, thermal transport may not be explained by turbulences or a model considered here.

3.3. Mixing and non-mixing states of hydrogen isotopes

In order to maximize fusion power in a future fusion reactor, a uniform mixture of D and T ions with a ratio of D/T = 1 is preferred. From a gyro-kinetic simulation, two states of isotope particle transport can be expected in isotope mixture plasmas, where isotope species exhibit freedom in a quasi-neutral condition, because this can be a constraint in evaluating ion densities, when charge numbers of ions are different but cannot be a constraint when the charge numbers are same and mass numbers are different [41]. The first state is an ITG dominant case, wherein the particle diffusivity of the ion (D_i) is larger than that of the electron (D_e). In this case, a large ion particle transport is expected, and the radial density profile of different isotope species will become the same, regardless of their source location, i.e. the isotope mixing state. The second state is the trapped electron mode (TEM) dominant case, wherein the D_e is larger than the D_i . In this case, a small ion particle transport is expected, and the radial density profile of these species can be different, depending on their source location, i.e. the isotope non-mixing state. These cases are crucial issues for controlling fusion power in reactors. Thus, investigating the behavior of mixing/non-mixing states of hydrogen isotopes and their relation to the turbulence in plasmas is important.

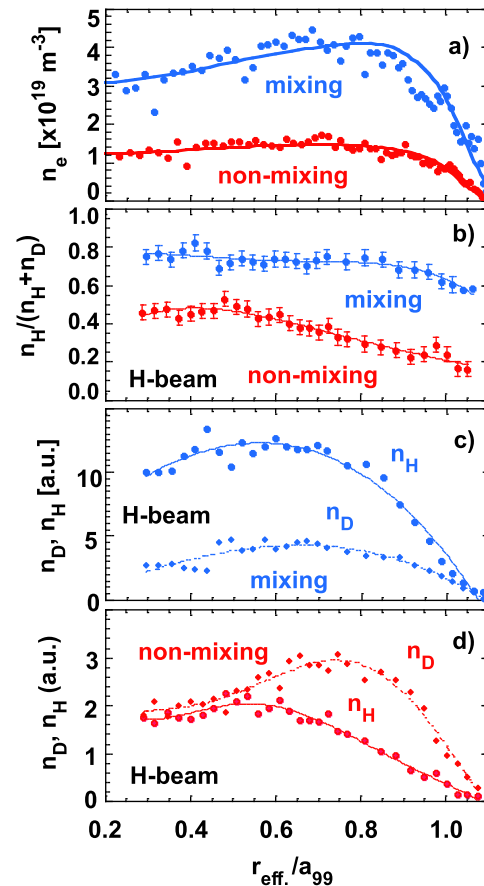


Figure 9. (a) Electron density profile, and (b) hydrogen fraction profiles for non-mixing (red lines with symbols) and mixing (light blue lines with symbols) cases shown. (c) Profiles of hydrogen (solid lines with circles) and deuterium (dashed lines with circles) ions for non-mixing case, and (d) hydrogen (solid lines with circles) and deuterium (dashed lines with circles) ions for mixing case also shown. (Reprinted figures from [42] with permission of IOP publishing).

In the LHD, a new diagnostic to evaluate the H/D ratio using CXS of bulk ions was developed and established [8]. The turbulence in plasmas can be evaluated through density fluctuation by a PCI diagnostic. The particle source location can be controlled using wall conditioning, ice pellets, and the NBI. Thus, the LHD is a good platform to explore this type of physics. Figure 9(a) shows typical electron density profiles for mixing (light blue lines) and non-mixing states of hydrogen isotopes (red lines). With low density plasma, a peaked density profile was observed for hydrogen, while the deuterium profile

was hollow, as shown in figure 9(d). This indicates the formation of a non-mixing state of hydrogen isotopes. The peaking of the hydrogen fraction at the core region is due to the combination of hydrogen NBI fueling at the core and deuterium dominated wall recycling ($\Gamma_D/\Gamma_H = 4$) at the periphery. Here, Γ_D and Γ_H are the influx (inward radial flux of deuterium and hydrogen neutrals) evaluated from H_α and D_α intensity, measured with passive spectroscopy. When the electron density is high, the density profiles of hydrogen and deuterium are similar, as shown in figure 9(c), and the profile of the hydrogen fraction, i.e. $n_H/(n_H + n_D)$, is flat except at the periphery, as shown by light blue lines in figure 9(b). The increase of the hydrogen fraction is attributed to the increase of hydrogen recycling ($\Gamma_D/\Gamma_H = 1.2$) but the flattening of the hydrogen fraction profile is due to the isotope mixing state. Note that an ice pellet injection does not play a role in particle fueling in the profile shown here. The ion temperature profiles are similar to each other and the central ion temperature ($T_i(0)$) is about 1.7 keV. The electron temperature is higher in a non-mixing case, where the central electron temperature ($T_e(0)$) is ~ 4 keV, than in a mixing case, where $T_e(0)$ is ~ 3 keV. Thus, the T_e/T_i ratio is higher for the non-mixing state than for the mixing state [42]. It has to be mentioned that the intrinsic toroidal rotation of co-direction is observed in the non-mixing state and that of the counter direction is observed in the mixing state [42].

The clear difference in the turbulence spectra between these two plasmas are also observed in figure 10, where red lines and light blue lines indicate observed turbulence spectra in the non-mixing and mixing state, respectively. The spectra are obtained from 2D-PCI signals and are integrated in the real space in the region of $r_{\text{eff}}/a_{99} > 0.4$ and also in the wave number (k) space in the region of $0.1 \text{ mm}^{-1} < k < 0.8 \text{ mm}^{-1}$. Here, the background level of the PCI diagnostic is subtracted by using the signal at the no-plasmas phase. The characteristic frequencies of the fluctuation in non-mixing state are 40–100 kHz and the fluctuation has a peak at ~ 80 kHz. The observed turbulence in non-mixing state resembles the quasi-coherent modes (QCMs), which is a type of TEM, observed in HL-2A and J-TEXT ohmic plasmas and in KSTAR ECH plasmas [42–44]. The observed frequency range of the QCM at HL-2A and J-TEXT is similar, i.e. 30–140 kHz. The QCM appears at a low collisionality (low density) range and a higher T_e/T_i ratio in these machines, as is similar to the non-mixing state. In the Alcator C-mod, the TEM turbulence is observed when the direction of intrinsic toroidal flow is co-direction and this TEM turbulence disappears, associated with the flow reversal from co-direction to counter-direction, which demonstrate that TEM drives the intrinsic toroidal flow in co-direction [45]. Thus, the existence of intrinsic flow in co-direction could be an indication of the TEM turbulence [42]. The density fluctuation in the mixing state has a peak at 25 kHz and its frequency range is 0–50 kHz, as shown in figure 10.

Linear growth rates of turbulence at the core, i.e. $r_{\text{eff}}/a_{99} = 0.5$, and at the edge, $r_{\text{eff}}/a_{99} = 0.9$, are calculated by GKV code for the non-mixing and mixing state, as shown in figure 11. The PCI diagnostic shows that the peak of the wave number of density fluctuation is $\sim 0.3 \text{ mm}^{-1}$. The linear growth rates for the wave number of $k_\theta = 0.2\text{--}0.4 \text{ mm}^{-1}$ are

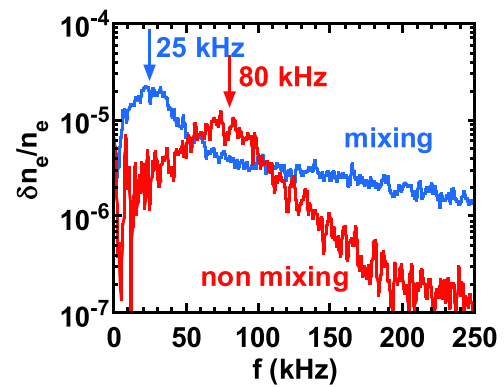


Figure 10. Results of density fluctuation measurement by PCI for discharges shown in figure 9. Red lines for non-mixing and light blue lines for mixing cases. (Reproduced courtesy of IAEA. Figure from [43]. Copyright (2021) IAEA.)

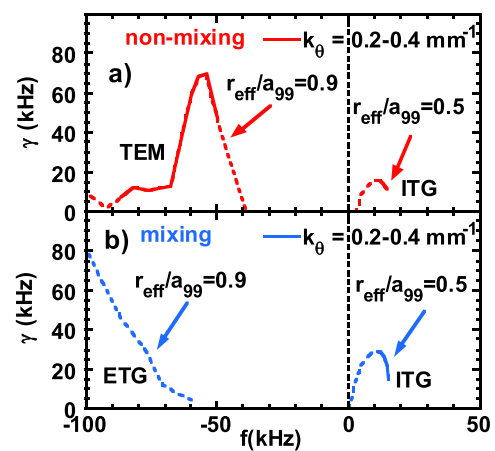


Figure 11. Linear growth rates of turbulences evaluated by GKV code at $r_{\text{eff}}/a_{99} = 0.5$ and 0.9 . Red lines and light blue lines indicate growth rates for non-mixing and mixing states, respectively. Solid lines indicate growth rates in k_θ range between 0.2 and 0.4 mm^{-1} , while dashed lines correspond to other wave numbers, i.e. $k_\theta < 0.2 \text{ mm}^{-1}$ and $k_\theta > 0.4 \text{ mm}^{-1}$. (Reproduced courtesy of IAEA. Figure from [43]. Copyright (2021) IAEA.)

plotted with a solid line in order to indicate the range for the density fluctuations measured by the PCI. In the non-mixing state, TEM is destabilized at the edge, where electron density and temperature are relatively sharp, and ITG is destabilized in the core region, where density gradient is positive (hollow profile). Conversely, in the mixing state, TEM is stabilized near the edge and ITG is still destabilized in the core. In the mixing state, the electron temperature gradient (ETG) mode is also destabilized near the edge. Because the wave number of the ETG, i.e. $k_\theta > 0.4 \text{ mm}^{-1}$, is greater than that of TEM, the ETG is not observed by the PCI diagnostic [42].

Typical characteristics of the isotope non-mixing and mixing state are summarized in table 2. The plasma parameters preferable for the non-mixing state are (1) lower collisionality, (2) higher T_e/T_i ratio, and (3) negative or zero density gradient, i.e. peaked or flat density profile, where TEM is expected to be destabilized. The preferable parameters for the mixing-state is higher collisionality, lower $T_e/T_i \sim 1$, and positive

Table 2. Typical characteristics of plasmas with isotope non-mixing and mixing state [38].

Parameters	Non-mixing state	Mixing state
Isotope density ratio	Non-uniform	Uniform
Electron density	$< 2-3 \times 10^{19} \text{ m}^{-3}$	$> 2-3 \times 10^{19} \text{ m}^{-3}$
Density gradient	$dn_e/dr_{\text{eff}} \leq 0$	$dn_e/dr_{\text{eff}} > 0$
T_e/T_i ratio	Large ($> 1-2$)	Small ($< 1-2$)
Peak frequency	60–90 kHz	20–40 kHz
Intrinsic toroidal flow	Co-direction	Counter-direction

density gradient, which can be produced by shallow pellet injection [42]. The strong correlation between isotope mixing and turbulence was observed in the LHD. The density fluctuation peaked at ~ 80 kHz was observed in the plasma with the non-mixing state, while this peak disappeared in the plasmas with the mixing state. It was difficult to identify the turbulence mode from the spectrum of density fluctuation. However, significant differences in density fluctuation spectrum observed between isotope mixing and non-mixing states demonstrate that the observed change in turbulence is a strong candidate for the mechanism causing the transition between isotope mixing and non-mixing states. By the GKV code, it was found that TEM can be destabilized near the plasma edge, due to a large density gradient and the ITG can be destabilized in the core region. The ITG in the core region is destabilized both for non-mixing and mixing states. TEM is destabilized in the non-mixing state and stabilized in the mixing state, which suggests that TEM contributes to the non-mixing state, where $D_e \gg D_i$ is expected [46].

4. Suppression of the EIC and its effect on EP transport

4.1. Suppression of the EIC

As mentioned in section 2, the loss of EPs by the EIC is a significant obstacle in extending high temperature plasmas in the LHD. Thus, we are trying to find a way to suppress the EIC. There are three conditions for the excitation of the EIC, i.e. (1) the marginally unstable status of the $n/m = 1/1$ RIC, (2) interaction between EPs and MHD instabilities through the resonant process, and (3) a sufficiently large EP pressure gradient. Therefore, if we can remove one of these three conditions from the high temperature discharge, we can suppress the EIC. However, the purpose of the suppression is to increase the effective heating power by EPs through the avoidance of its loss. The reduction of an EP population to reduce its pressure gradient is out of our scope. Thus, we exclude the third condition. Figure 12(a) shows a stability diagram of the EIC as a function of the local temperature and density at $\iota = 1$, surface evaluated by FAR3d code [12, 19, 47]. The $\iota = 1$ surface locates at the edge of the LHD, e.g. its location corresponds to $r_{\text{eff}}/a_{99} = \sim 0.9$ in #150141 of figure 2. It was found that the stability of the EIC is closely related to the dumping effect of the Alfvén wave, whose frequency decreases with increasing electron density. Thus, the EIC becomes unstable

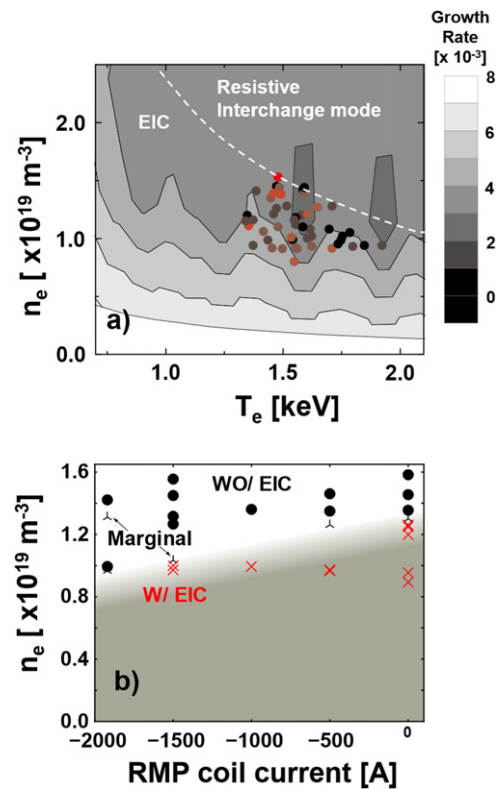


Figure 12. (a) Stability diagram of EIC as function of local temperature and density. Colored circles show plasma parameters when EIC is observed and color of circles indicate amplitude of EIC (small: black to large: red). Dashed lines show boundary between dominant $n = 1/m = 1$ EIC to RIC. (b) Threshold density to excite EIC as function of RMP coil current. ((a) and (b) Reproduced with permission from [12].)

for the low-density regime, and the existence of a density limit for its excitation is expected, as shown by dashed curves in figure 12(a). Pairs of plasma parameters (n_e and T_e) when EIC bursts are observed are plotted as circles in figure 12(a). The upper bounds of the plotted circles seems to be consistent with the expected EIC excitation boundary. At high electron temperature regimes, two effects simultaneously affect the stability of the EIC. One effect is the change of resistivity and Alfvén gap structure. This was considered using FAR3d [19, 47]. The other effect is the reduction of the width of the mode structure, which is proportional to $T_e^{-1/2}(\beta dp_e/dr_{\text{eff}}/p_e)^{1/6}$ [18]. The reduction of a width smaller than the orbit width of helically trapped EPs will reduce the chance of EPs to resonate with the EIC. This effect was not considered in FAR3d and was not included in figure 12(a). Figure 13 shows a comparison of EIC activities and associated EP confinement with and without ECH superposition. As shown in figure 13(b), the neutron emission rate drops with EIC bursting activity. This indicates the loss of EPs by the EIC. As can be seen in figure 13(c), the number of EIC activities is reduced by the application of ECH, and the neutron emission rate becomes larger than the case without RMP. Thus, the application of the ECH, is a useful tool to suppress the EIC [12].

As another tool for controlling the EIC, the RMP for $m/n = 1/1$ island formation was examined. Application of

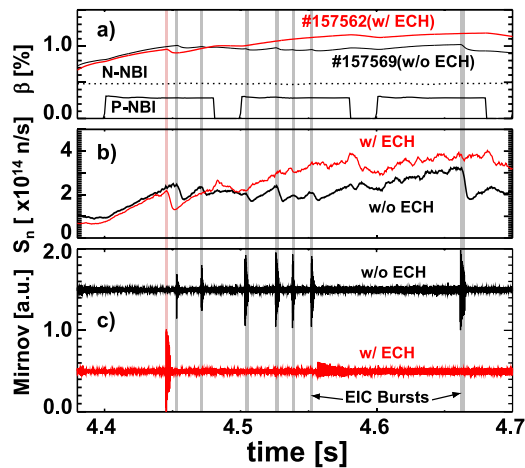


Figure 13. Temporal evolution of (a) β and timing of NBI heating, (b) total neutron emission rate, and (c) magnetic fluctuation measured by Mirnov-coil. Black lines correspond to discharge without ECH superposition, while red lines correspond to discharge with ECH suppression. ECH superposed from 4.3 s through 5.3 s in #157569. (Reproduced with permission from [12].)

RMP is known to stabilize the RIC mode, which is considered as a seed instability of the EIC. The original aim of RIC stabilization by RMP application is to reduce the pressure gradient of bulk plasmas at $iota = 1$ surface by forming a magnetic island; although it was found that the RIC could be suppressed even if an island was not formed due to the plasma response at a low RMP coil current setting [48]. Figure 12(b) shows pairs of electron line average density and RMP-coil current. When an EIC is observed, the pair is plotted as a red cross. Conversely, the pair is plotted as a black circle when an EIC is not observed. As shown in figure 12(b), the threshold density where the EIC disappearance can be controlled by the applied RMP current, i.e. the threshold density decreases as the absolute value of the applied RMP coil current increases [12]. This figure indicates RMP can be used to control the EIC disappearance, but it must be noted that application of too much RMP coil current is not preferable in extending the high temperature domain of LHD plasmas, because an application of a large RMP coil current could cause a flattening of electron temperature at $iota = 1$ surface through an island formation. This results in the reduction of electron temperature and the decrease of the EP population through the decrease of energy slowing-down time. Thus, an applied RMP coil current must be chosen carefully so that it reduces the threshold for RIC onset, without deteriorating the electron temperature profile, as shown in [45]. Optimization of RMP application with ECH superposition is ongoing to extend the high-temperature domain of the LHD.

4.2. Influence of the EIC on EPs

The interactions between EPs and EP-driven instabilities are of great interest. A significant loss of up to 60% of EPs, which are produced by radial NBI, by the influence of the EIC, were reported [13]. Recently, the influence of the EIC on energetic triton produced by the D–D fusion reaction was also observed, as shown in figure 14 [11]. Figures 15(a) and (b)

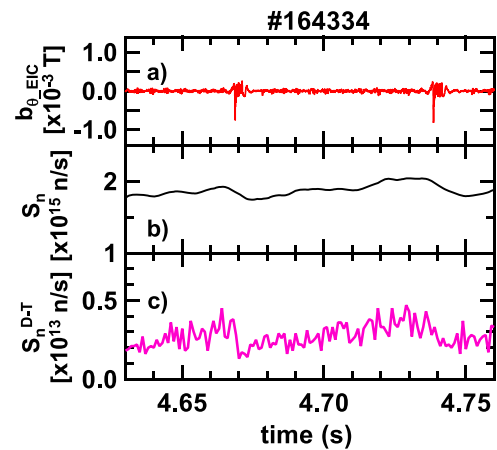


Figure 14. Waveforms for discharge (#164334) where loss of triton produced by D–D reaction observed. (a) Magnetic fluctuation measured by Mirnov-coil, (b) D–D neutron emission rate, and (c) D–T neutron emission rate shown [11]. During this time interval all NBs injected with deuterium atoms at port-through power of ~ 3 MW (NB#1), ~ 1.5 MW (NB#2), ~ 2 MW (NB#3), ~ 8 MW (NB#4), and ~ 9 MW (NB#5). (Reproduced from [11]. © 2021 IAEA. CC BY 4.0.)

show the mode amplitude dependence of the neutron emission drop rates for D–D and D–T reactions [11]. It is noted that the data shown in figure 15(a) are obtained when the N-NBIs, which are tangentially injected, are operated with hydrogen while positive-ion based NBIs (P-NBIs), which are radially injected, are operated with deuterium. Thus, the D–D neutrons are produced by helically trapped energetic deuterons. We also note that the reactant triton energy of the D–T reaction is around 100 keV because the cross section of the reaction is maximized at ~ 100 keV, although the initial energy of triton is about 1 MeV. It was found that the drop rate of the D–D neutron emission rate is almost linearly correlated to the mode amplitude of the EIC ($b_{\theta,EIC}$). This indicates the loss of deuteron is the convective type [11, 49]. As shown in figure 15(b), 30% of the triton might be lost by the influence of the EIC, and the drop rate of the D–T neutron emission rate roughly correlates to $b_{\theta,EIC}^3$. The exponent of the mode amplitude to the drop of the D–T neutron emission rate is three. This indicates that the loss of triton is much more sensitive to the EIC mode activity, compared to that of deuteron. This might be due to the triton Larmor radius being much larger than that of the deuteron produced by the P-NBI, whose injection energy is 80 keV. The Lorentz orbit of triton produces a stochastic layer around its drift orbit surfaces for EPs, due to the effect of the finite Larmor radius with various gyro-phases, as shown in figure 16. Because the width of stochastic layer for 1 MeV triton is much wider than that of 80 keV deuteron, the loss boundary of the triton locates more on the inner side of plasmas than that of the deuteron. Thus, a small radial excursion of EPs by the interaction with the EIC could result in a more significant EP loss for the 1 MeV triton than the 80 keV deuteron. Therefore, the formation of these stochastic layers by the finite Larmor radius effect makes the triton orbit more sensitive to the magnetic field perturbation caused by the EIC [11].

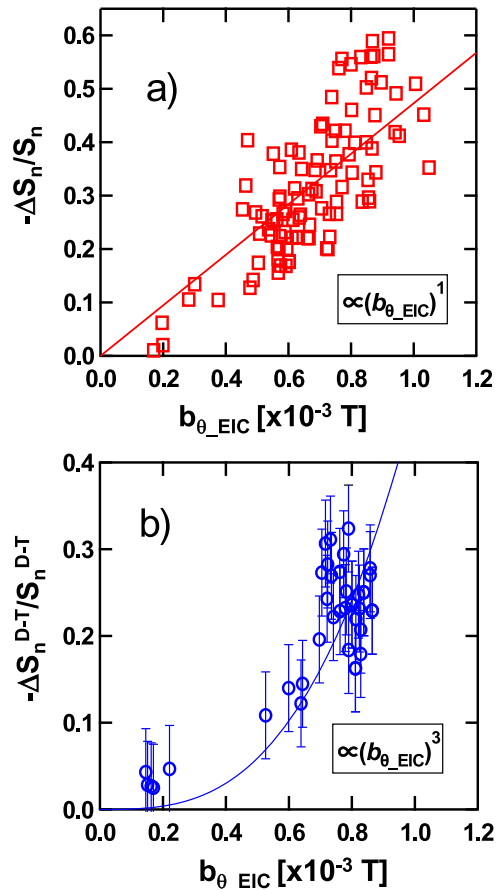


Figure 15. (a) EIC mode amplitude dependence of drop rate of neutron emission rates for D–D and (b) D–T reaction shown. (Reproduced from [11]. © 2021 IAEA. CC BY 4.0.)

5. Realization of divertor detachment and confinement improvement

confinement. Because a stable divertor detachment is realized by the application of an RMP of $n/m = 1/1$ and the improved confinement is associated with the formation of an ETB, we call this improved confinement mode the RMP induced H-mode [16]. Figure 17 shows typical waveforms of a discharge wherein an RMP induced H-mode was observed. In this discharge, the density was ramped up using deuterium gas. Radiation mainly originated from the carbon impurity generated by sputtering of the graphite tiles at the divertor plates. No additional impurities were seeded to enhance radiation. As shown in figure 17(d), detachment occurs at $t = \sim 3.95$ s, and the reduction of particle flux to the divertor is observed. The particle flux was measured by a sum of ion saturation currents from 20 channel Langmuir-probes which were installed at a single divertor tile to monitor the particle flux profile. During the detachment phase, the electron density exceeds the Sudo density limit [50], as indicated by dashed lines in figure 17(a) and the radiation power from the plasma reaches $\sim 60\%$ of the input power at $t = \sim 4.2$ s, as shown in figure 17(b). Increase of plasma stored energy ($W_p^{\text{dia.}}$) is observed at the onset of

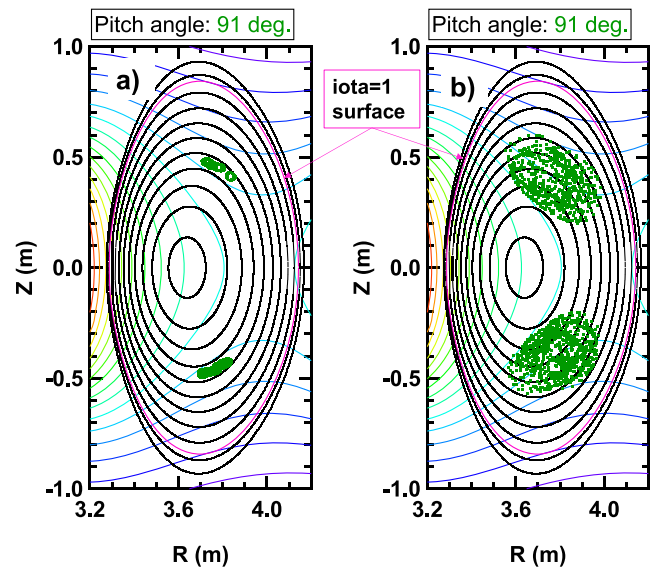


Figure 16. Typical Poincare plots of helically trapped particles' orbit are shown by green dots for (a) deuterium beam ions of 80 keV and (b) triton of 1 MeV at vertically elongated poloidal cross section [11]. Magnetic configuration of $R_{ax} = 3.6$ m and $B_t = 2.75$ T on axis adopted. Particle launched from point $(R, Z) = (3.7 \text{ m}, -0.5 \text{ m})$ with pitch angle of 91 degree. Orbit calculation performed for one helical section with periodic boundary condition. Black and pink elliptic curves indicate magnetic surfaces, while colored curves, except pink elliptic curves, show contours of magnetic field strength. From red to purple via light blue, magnetic field strength becomes weak. Pink elliptic curve indicates magnetic surface of $\iota = 1$. (Reproduced from [11]. © 2021 IAEA. CC BY 4.0.)

detachment at $t = \sim 3.95$ s. Stable sustainment of the detachment and the enhanced radiation becomes possible by application of the RMP. This enhancement of radiation is due to the formation of a stochastic layer around the $\iota = 1$ surface by the RMP. As shown in figures 17(f) and (g), a flat low temperature region below ~ 20 eV is formed at the region of $L_c < 10^4$ m with the detachment onset. The expansion of the volume with this low temperature range significantly enhances the radiation from impurity ions. After the onset of the detachment, we also observe another increase of plasma stored energy at $t = \sim 4.55$ s. This second increase in stored energy causes an increase of pressure gradient at the ETB, resulting in the formation of an improved confinement mode, i.e. the RMP induced H-mode, as shown in figure 18(a). An improvement in τ_E of 38% was observed during this phase. The expanded electron pressure, temperature, and density profiles are also shown for the outboard peripheral region in figures 18(c)–(e), respectively. As shown in these figures, the steep gradient is observed during the attached phase, only in temperature profile not in density profile, resulting in a modest pressure gradient formation at the confinement boundary, where the steep gradient in L_c is formed. At the onset of detachment, a steep gradient in density profile is formed in the region $R = 4.52$ m and 4.64 m, while the steep temperature gradient is formed more in the inner region of the plasma. The formation of steep gradient regions at different locations suggests the decoupling between thermal and particle confinement properties. In tokamak plasmas, the decoupling of these confinement properties

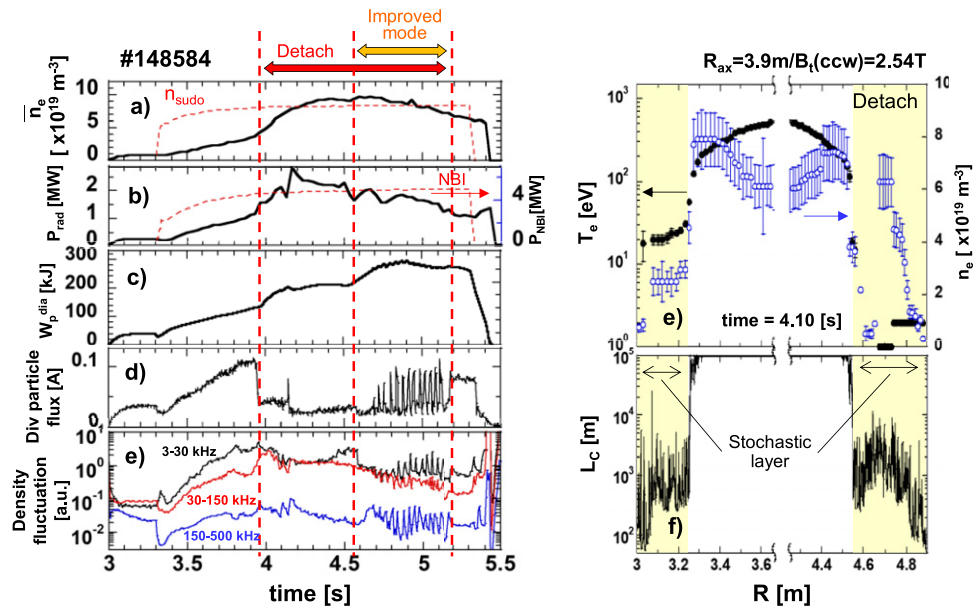


Figure 17. Temporal evolution (a) line averaged density (black solid), Sudo density (red dashed) (b) radiation power (black solid), NB deposition power (red dashed), (c) diamagnetic stored energy, (d) divertor particle flux, (e) density fluctuation measured by PCI for 3–30 kHz (black), 30–150 kHz (red), and 150–300 kHz (blue). (f) Electron density and temperature profile at detached phase ($t = 4.1$ s) and (g) profile of magnetic field line connection length (L_c). (Reproduced with permission from [16].)

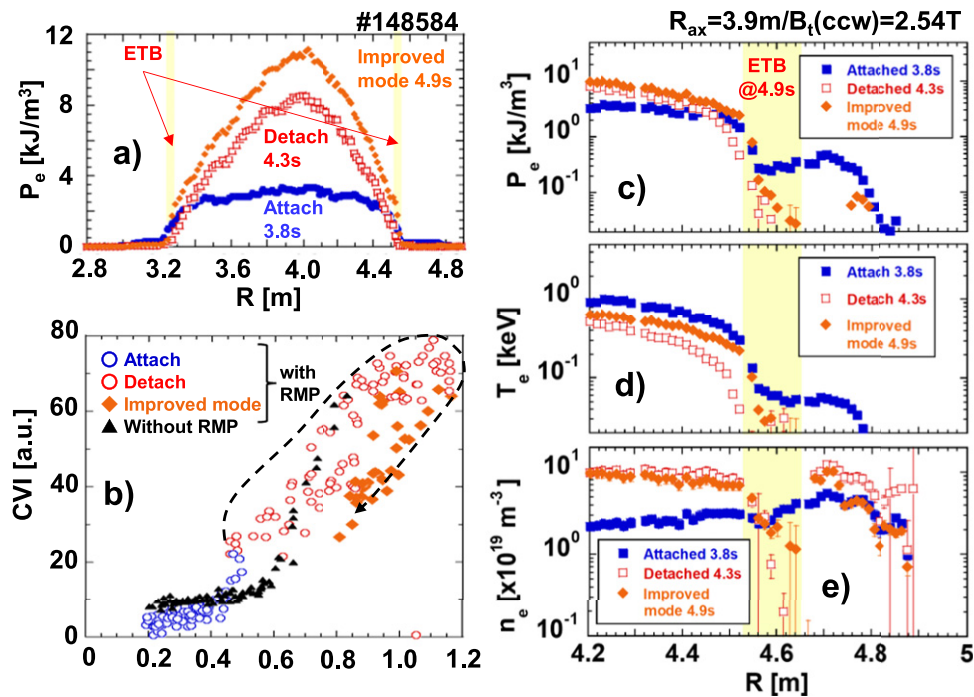


Figure 18. (a) Pressure profiles of attached case (blue), detached case (red) and improved confinement with detachment case (orange) shown. (b) Carbon emission intensity (CVI (1s- 2p, 3.4 nm) as function of line averaged density normalized by density limit. Dashed curves with arrow indicate temporal evolution during discharge with RMP. Expanded plots of electron (c) pressure, (d) temperature, and (e) density profiles also shown with similar manner as cases in (a). Yellow hatched areas in these figures indicate ETB region during improved mode. ((b) Reproduced with permission from [16].)

by the influence of the RMP field is also pointed out, resulting in the formation of I-mode in the Alcator-C mod and particle enhanced H-mode in the DIII-D [51]. At the onset of the RMP induced H-mode, the steep gradient regions in temperature and density profiles match each other. The increase of the

pressure gradient at the ETB also triggers the edge localized mode (ELM) from $t = \sim 4.7$ s, as shown in figure 17(d). During this improved confinement mode, a reduction of impurities is observed, as shown in figure 18(b). This reduction leads to the increase of the divertor heat load, in addition to ELM activ-

ities. The triggering mechanism for the RMP induced H-mode is not clear and its investigation is ongoing. One hypothesis of the mechanism is that the parallel flow enhancement along the separatrix of the $n/m = 1/1$ island and its associated shear flow generation might trigger the RMP induced H-mode, where the enhanced parallel flow is induced by the radiative cooling at the x -point during the divertor detachment [16, 52].

6. Engineering contribution to fusion reactor development

6.1. Research and development of a negative-ion source for the NBI

An N-NBI is an inevitable heating and current drive device for the ITER and future fusion reactors based on the tokamak concept. The LHD is the only machine that has operated multiple N-NBIs and demonstrated their reliable operation for more than 20 years, as shown in figure 19(a). The N-NBI has been in operation since 1998 on the LHD with two injectors [53]. The third injector was installed and began operation in 2001. The injection power of the N-NBI was far below the nominal injection power of 5 MW in the first year of operation and gradually increased year-by-year, with improvements in voltage holding capability and negative-ion production efficiency. In 2007, we succeeded in exceeding the nominal injection power. Moreover, one NBI achieved 6.6 MW with an injection energy of 190 keV. Figure 19(b) shows the achieved negative-ion current density by the ion source of this NBI. As can be seen in this figure, a current density of 342 A m^{-2} , which is far above the specification of the ITER-NBI, was achieved by the ion-source. The minimum beam divergent angle achieved by this ion-source is 4.1 mrad in the horizontal direction and 6.1 mrad in the vertical direction, where a single beamlet shows an elliptical shape due to the slotted shape of the grounded grid of the sources [54, 55]. This achievement also fulfills the requirement of the ITER-NBI for a beam divergent angle of 3–7 mrad. In the negative-ion source, electrons are extracted from the ion-source plasma with negative-ions because the ion-source is negatively biased. The fraction of electron beam current to the extracted negative-ion beam, which is called the ‘co-extracted electron fraction’, is also an important parameter for an N-NBI because the extracted electron is the source of heat load onto the grid system of the ion-source and its increase could damage the grid. For the ITER-NBI, a co-extracted electron fraction below unity is required, while 0.25 is achieved in the LHD-NBI. In table 3, parameters achieved by the LHD-NBI are summarized and compared to the ITER-NBI requirements. As can be seen in this table, the three parameters in the ITER-NBI requirements are simultaneously fulfilled by the LHD-NBI. This fact, together with the demonstration of reliable operation of the LHD-NBI over twenty years, strongly supports the adoption of an N-NBI as the main heating and current drive device for the ITER and future fusion reactors.

Deuterium beam operation began in 2017 with the start of deuterium experiments in the LHD. By starting deuterium operation of a negative-ion source, we recognized the isotope effect in negative-ion beam production, i.e. the increase of the

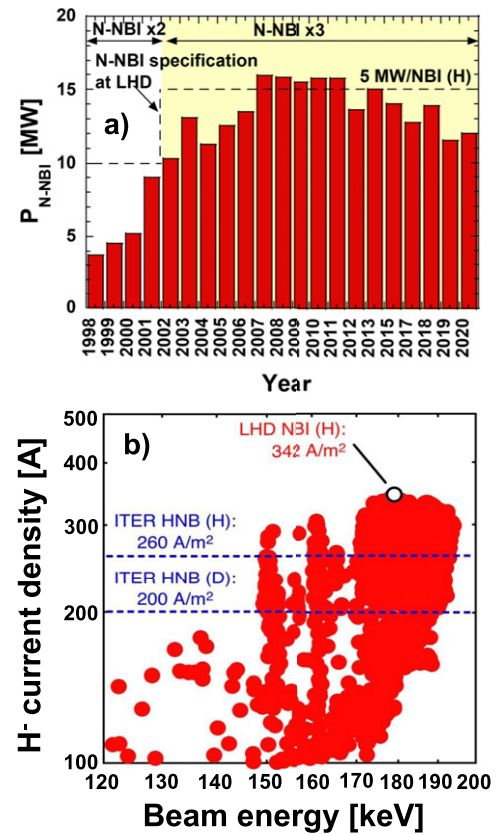


Figure 19. (a) History of maximum total injection power and (b) achieved negative-ion current density by N-NBIs in LHD. Both results with hydrogen operation.

Table 3. Requirement of N-NBI for ITER and achievement at LHD-NBI for current density (J_{H-}), co-extracted electron fraction to negative ion (I_e/I_{H-}), and divergent angle (θ_{div}).

	ITER-NBI	LHD-NBI(H)
J_{H-}	$>260 \text{ A m}^{-2}$	340 A m^{-2}
I_e/I_{H-}	<1	0.25
θ_{div}	3–7 mrad	5 mrad (average), 4 mrad (horizontal) \times 6 mrad (vertical)

co-extracted electron fraction with the change of ion species from hydrogen to deuterium. We found that the co-extracted electron fraction increases from $\sim 25\%$ in hydrogen to $\sim 40\%$ in deuterium [2, 56]. In order to avoid damage to the grid, which might be caused by the increase of the co-extracted electron, the total extraction beam current must be reduced. Thus, reducing the injection power of the N-NBI for the deuterium operation to almost half that of the hydrogen operation was necessary. To reduce the co-extracted electron fraction during the deuterium operation without deteriorating the performance during the hydrogen operation, several methods, e.g. shortening the gap distance between grids [56], installing an ‘electron fence’ at the vicinity of the beam extraction region of ion-source plasmas [57], etc. were conducted. These methods demonstrate preferable effects in mitigating the isotope effect in negative-ion production, and the beam injection power for

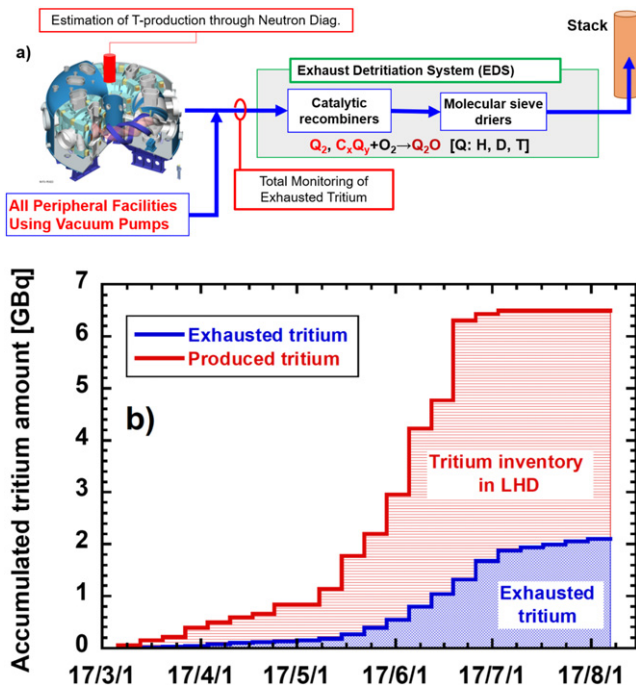


Figure 20. (a) Schematic diagram of tritium mass balance monitoring in the LHD deuterium experiment. (b) Total tritium inventory (red lines) in LHD and total tritium exhausted (blue lines) by vacuum pump for first deuterium campaign. ((b) [60] 24 June 2020, reprinted by permission of the publisher (Taylor & Francis Ltd, <http://www.tandfonline.com>.)

the deuterium operation was improved from $\sim 50\%$ of the power in the hydrogen operation to $\sim 60\%$, which becomes closer to the limit of beam extraction current by mass through the Child–Langmuir law, i.e. (beam current) $\propto M^{-1/2} \sim 70\%$.

6.2. Tritium mass balance study

The mass balance of tritium in a single fusion reactor is a crucial issue for developing a future fusion reactor fuel cycle. Especially, the evaluation of tritium consumption other than D–T fusion reaction, i.e. retentions in the VV of the reactor torus, peripheral devices, and vacuum components of a fusion reactor are important. In deuterium experiments, the amount of tritium produced in plasmas can be accurately evaluated from neutron diagnostics because the branching ratio of $D(d, n)^3\text{He}$ and $D(d, p)\text{T}$ reactions can be considered as constant, e.g. the ratio can be almost unity in many cases. Thus, the D–D fusion born tritium is often used as a tracer particle to investigate the tritium retention fraction and mass balance studies for future fusion reactors [58–61]. In many cases, only the tritium exhausted by the vacuum pumping system of a torus is monitored although certain fraction of the tritium is evacuated through the peripheral facilities, i.e. NBIs and diagnostic systems which are directly connected to the VV of the torus with their connection ports. The fraction of tritium evacuated through the peripheral facilities becomes an ambiguity in mass balance evaluation. In the LHD deuterium experiment, tritium produced by the D–D fusion reaction is evaluated by absolutely calibrated measurement of neutrons

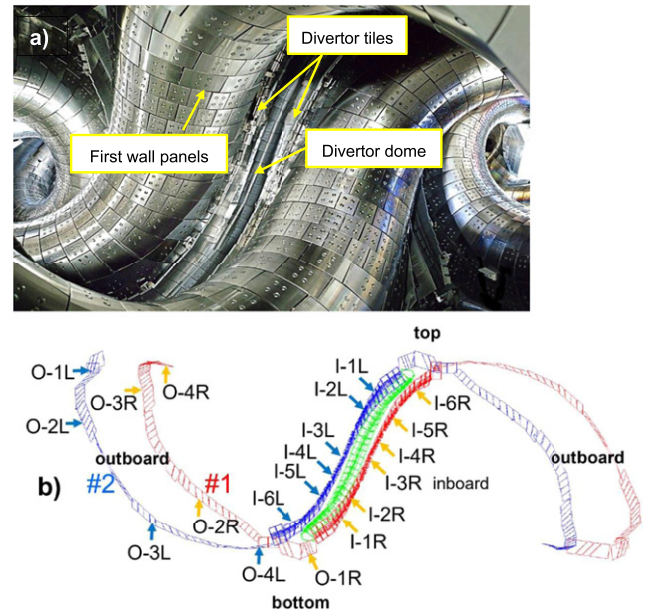


Figure 21. (a) Photograph of inboard side of LHD-VV, and (b) Schematic drawing of divertor tile arrays of LHD. Divertor tiles to which TIPT was applied indicated by arrows with tile index, i.e. I-1L. ((b) Reproduced from [65]. © 2020 The Royal Swedish Academy of Sciences. All rights reserved.)

produced by the D–D fusion reaction. The total tritium content in the vacuum exhaust from the LHD vacuum vessel and all of the peripheral facilities are monitored at the inlet of the exhaust detritiation system (EDS), as shown in figure 20(a). Thus, the LHD deuterium experiment is a good platform for the evaluation of tritium mass balance in a plasma confinement device. Figure 20(b) shows the tritium inventory and total exhausted tritium during the first deuterium campaign. As shown in this figure, a total of 6.4 GBq of tritium was produced and 2.1 GBq was exhausted through the vacuum pumping system during the period [62, 63]. Thus, the remaining 4.3 GBq of the tritium is in the vacuum vessel of the LHD. We also estimated the remaining tritium in the divertor tiles as ~ 2 GBq, which corresponds roughly half of the remaining tritium in the LHD-VV evaluated by the exhaust gas monitoring. The detail of the estimation is shown later in this section. It has to be mentioned that the uncertainty of tritium inventory evaluation is about 10%, which comes from the accuracy of neutron diagnostics which are used to evaluate the tritium production rate, assuming this production rate is equal to the neutron emission rate in the D–D fusion reaction [64–66].

Because NBIs have the largest influences on the pumping of the LHD-VV among the peripheral facilities, except the vacuum pumping system of the LHD. Thus, NBI-VVs could contain a part of the remaining tritium. Activated charcoal panels of cryo-sorption pumps in NBI-VVs are considered to be the largest reservoir of the tritium in NBI-VVs, because these panels are used as vacuum pumps by absorbing hydrogen isotopes during the operation of NBIs. Several pieces of charcoal were sampled after the first deuterium campaign and the remaining tritium in the charcoal was measured by the water immersion method. From this measurement, the total inventory in

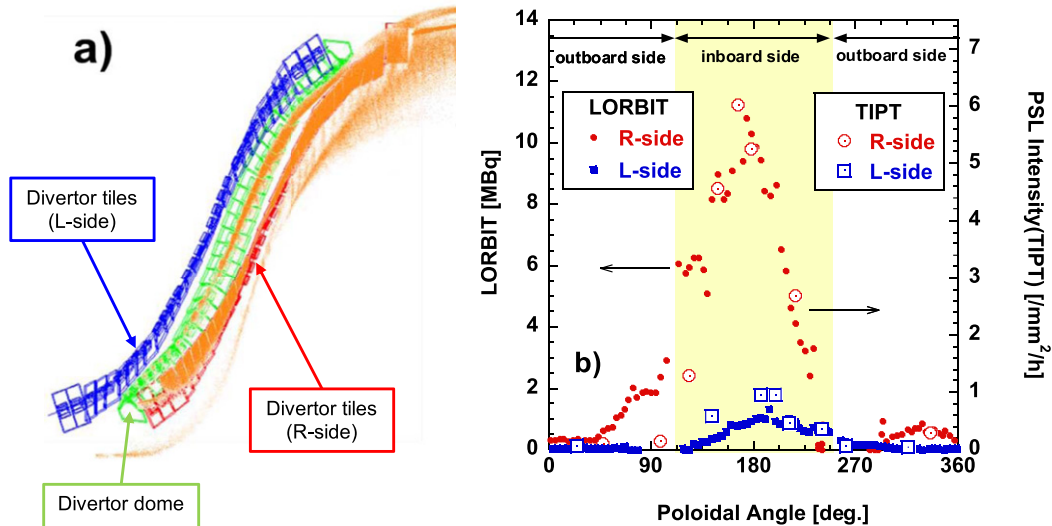


Figure 22. (a) Loss points of energetic tritons at inboard-side of LHD-VV shown by orange dots. Objects shown by blue, and red left and right divertor tile arrays, respectively. Those shown by green dome of divertor. Here, the toroidal magnetic field direction chosen CCW direction, so NBI#1 and NBI#3 become co-injection in calculation. (b) Evaluated total amount of tritium impinged to divertor tiles during first deuterium campaign by LORBIT-code (small closed symbols) and measured tritium distribution by TIPT (large open symbols). Each symbol represents piece of divertor tile. Red and blue symbols for right and left divertor tiles, respectively. ((a) Reprinted from [66], Copyright (2021), with permission from Elsevier. CC BY-NC-ND 4.0.)

the charcoal panels was estimated to be ~ 3 MBq, which corresponds to less than 0.1% of the produced tritium [63]. Thus, the contribution of remaining tritium in peripheral devices to the total inventory is considered to be negligible.

To investigate the remaining tritium in the vacuum vessel, the tritium content in the plasma facing components (PFCs), i.e. the divertor tiles and the first wall panels (FWPs) of the vacuum vessel, is now under investigation using tritium imaging plate technique (TIPT) [67–70]. Divertor tiles are made of carbon, while the FWPs are made of a stainless steel and copper composite on the LHD. Figure 21(a) shows a picture of the inboard-side of the LHD-VV. As shown in this figure, divertor tiles are installed in the region between two helical coils and FWPs are placed to protect helical coil cans. Twelve divertor tiles (I-1L–6L and I-1R–6R) from the inboard divertor region and four divertor tiles (O-2L, 3L, 2R and 3R) from the outboard region in one helical section were selected to apply the TIPT, as shown in figure 21(b) [67]. For the divertor tiles, a full combustion method is also applied to evaluate tritium impinging deeper than the escape depth of β -rays from tritium decay [69, 70]. Two FWPs, which are next to the divertor tiles and one from the top and the other from the bottom part of the LHD-VV, are also selected to apply the TIPT [67]. To sample the tritium on the surface of FWPs more easily than to directly measure FWP surfaces, twenty-six material probes, which are pieces of small stainless-steel plates and are made of same material as the FWP surface, were placed on the surface of FWPs at various locations [67, 70]. The largest remaining tritium amount of 0.5 GBq m^{-2} was observed among measured divertor tiles, while that of 0.6 MBq m^{-2} was observed among measured FWP surfaces and material probe surfaces [70]. It was found that the tritium remains mainly in the divertor tiles.

To evaluate the distribution of tritium in the LHD-VV, the first-orbit loss points of energetic tritons, which were produced by the D–D fusion reaction, were calculated by a Lorentz orbit following (LORBIT) code, as shown in figure 22(a) [68, 70, 71]. In the orbit calculation shown in figure 22(a), the toroidal magnetic field direction was set in a counter clockwise (CCW) direction seen from the top of the LHD-VV and magnetic field strength was set to 2.75 T. As shown in the figure, the loss points of energetic tritons are concentrated at the right-side of the divertor region for CCW magnetic field configurations. Because the first orbit loss is dominated by the grad-B drift on the LHD, this loss region moves to the left-side of the divertor region when the magnetic field direction is set in a clock-wise (CW) direction [67, 70]. The distribution of tritium impinged on divertor tiles during the first deuterium campaign was estimated from the triton loss distribution, calculated by the LORBIT code for the CCW and CW of $R_{\text{ax}} = 3.6$ m configurations at 2.75 T, and assuming the distributions were similar to them for all magnetic field strength. The results of the calculation are shown in figure 22(b) with closed symbols, where the total amount of tritium produced for CCW and CW configurations are estimated from the measured neutron yield for CCW and CW configurations, during the first deuterium campaign. Distributions of tritium contained in divertor tiles were evaluated by the TIPT and are shown by open symbols in figure 22(b). In the TIPT, intensities of photo-stimulated luminescence (PSL), which are proportional to the intensities of β -rays emitted from tritium on the surface of measurement objects, are measured. As shown in the figure 22(b), the PSL intensity distributions are consistent with the first orbit loss distributions of energetic tritons [67–69], especially in the region of inboard right side divertor plates.

This indicates the evaluation of tritium distribution in a magnetic confinement device with a deuterium experiment can be used to validate the EP transport simulation. In figure 22(b) the triton loss calculation by the LORBIT code seems to overestimate the measured tritium distribution in a region of between 45 and 112 degrees in poloidal angle. This difference might come from the effect of EP collision with background plasmas, which are not considered in the LORBIT code. Assuming that the remaining tritium distribution in the LHD-VV is proportional to the impinged triton distribution evaluated by the LORBIT code and considering the measured remaining tritium evaluated by the TIPT and the combustion method, the total remaining tritium in the LHD-VV are estimated to be 2 GBq [70]. The tritium inventory in the LHD-VV by the remaining tritium measurement is about a half of that by the exhaust gas evaluation, i.e. 4.3 GBq. Further analysis and measurement are necessary for accurate evaluation.

7. Conclusion

Deuterium experiments have been conducted since March 2017. The high temperature domain of LHD plasmas was extended further, in both electron and ion temperatures, to explore the physics related to reactor-relevant plasmas. The $T_i = 10$ keV and $T_e = 6.6$ keV were successfully and simultaneously achieved. The suppression of the EIC is key to extending the high temperature domain as 60% of EPs, which mainly heat the ions of plasmas, can be lost by interaction with the EIC. It was found that the applications of RMP and ECH to high temperature plasmas are effective methods to suppress the EIC. The effect of the T_e/T_i ratio in extending the high ion temperature plasma domain was surveyed, and we found a threshold value of 0.75. Above this ratio, confinement properties of thermal ions are degraded. Considering these new findings, a moderate increase in electron temperature by ECH superposition is the most effective way to suppress the EIC and to expand the high T_i and T_e domains of the LHD.

Understanding the isotope effect is one of most important tasks in deuterium experiments. The scaling law for τ_E describing the isotope effect for L-mode plasma was extended to H, D, and their mixture plasmas. The scaling law of the confinement time normalized by ion gyro frequency ($\tau_E \Omega_i$) clearly shows mass (M) dependence on the exponent of near unity (0.94), in addition to the gyro-Bohm dependence of $\tau_E \Omega_i \propto M^0 \rho^{*-3}$, where the effective mass (M_{eff}) is used as M for mixture plasmas. Thermal diffusivity in dimensionally similar plasmas has also been compared to clarify the character of the isotope effect. It was found that the χ_e/Ω_i of hydrogen plasmas stayed almost twice as large as those of deuterium plasmas. This tendency exhibits the mass dependence in normalized global energy confinement time, i.e. $\tau_E \Omega_i \sim M^1$. It was also found that the improvement in χ_i/Ω_i for D plasmas is significant, especially for the low collisional region of $\nu^* < 0.2$. Conversely, the difference in χ_i/Ω_i is less significant when $\nu^* > 0.2$. The relative amplitude and k spectrum of density fluctuation were also surveyed for dimensionally similar H and D plasmas. The k spectrum of density fluctuation for H and D plasmas have a similar peak position and the amplitude is

smaller for deuterium plasma than hydrogen plasma. Coinciding reduction of density fluctuation and thermal transport was observed.

The ITB intensity was defined to qualitatively investigate the isotope effect for plasmas with an ITB. It was found that the ITB intensity exhibits a larger value for D-plasmas than for H-plasmas in the region, where both the ion heating power density (P_i/\bar{n}_e) and the inverse of the density scale length ($L_{n_e}^{-1}$) are large. To explore the physics underlying the ITB formation, a series of GKV simulations were performed to evaluate the linear growth rate of turbulences for hydrogen and deuterium ITB and L-mode plasmas. The tendency of an evaluated linear growth rate was consistent with the experimental observation in the difference between hydrogen and deuterium, but the tendency was not consistent with the experimental observation in the difference between ITB and L-mode plasmas. The results indicate the thermal transport may not be explained by the turbulences and/or model considered in the calculation.

To maximize the output power of a fusion reactor, it is preferred that the D and T ions are uniformly distributed with the ratio of D/T = 1. In other words, the mixture of hydrogen isotopes can be used as a tool for controlling fusion power without changing the performance of the plasmas. A theory suggests the mixing state will be observed when ITG turbulence is dominant, while the non-mixing state will be observed when TEM turbulence is dominant. The research for investigating the mixing/non-mixing states of the hydrogen isotope plasmas began with the LHD. Initial results suggest they are consistent with theoretical prediction.

The realization of both divertor heat load mitigation and good core confinement properties is an important issue for developing future reactor scenarios. The RMP is utilized to stabilize the detachment. A low temperature region, below the electron temperature of ~ 20 eV, was expanded in the stochastic region formed by the RMP coil. This expansion of the low temperature region enhances radiation power, reaching 60% of injection heating power. After the onset of detachment, improved confinement, called the RMP induced H-mode, was realized. Enhanced radiation at the X-point of an $n/m = 1/1$ island during the detachment might play an important role in the triggering RMP-induced H-mode.

The LHD is the only machine that has demonstrated a reliable operation of multiple N-NBIs for more than twenty years. It has also demonstrated that the three parameters of the ITER-NBI requirement, i.e. a negative-ion current density, co-extracted electron fraction, and beam divergent angle, can be fulfilled simultaneously. These demonstrations strongly encourage the adoption of N-NBIs as the main heating and current drive devices for future fusion reactors. The isotope effect in negative-ion beam production is recognized in N-NBIs of the LHD. Due to this effect, the beam injection power in the deuterium operation was limited to $\sim 50\%$ of that in the hydrogen operation during the first deuterium campaign of the LHD. Several methods were explored to mitigate the isotope effect. These methods successfully increased the injection power in deuterium operation from $\sim 50\%$ of the hydrogen operation to $\sim 60\%$, which becomes closer to the limit of beam extraction current by mass through the Child–Langmuir law, i.e. (beam

current) $\propto M^{-1/2} \sim 70\%$. This exploration in the mitigation of the isotope effect will also contribute to the development of N-NBIs for future fusion reactors.

A tritium mass balance study was performed using the installed EDS and required accumulation of the vacuum exhaust gases from not only the LHD-VV but also all of the peripheral facilities whose VVs were connected to the LHD-VV. A tritium mass balance was investigated for the first deuterium campaign. From exhaust gas analysis, 37.8% of the tritium produced by the D–D fusion reaction was found to be exhausted, and 57.2% of the tritium remained in the LHD-VV. The investigation of the remaining tritium in the LHD-VV was also performed through the measurement of tritium content in materials in the LHD-VV. The measurement showed that most of the tritium remained in the divertor tiles, not in the first wall. The largest amount of remaining tritium was 0.3 GBq m⁻² in the divertor tiles and 0.6 MBq m⁻² in the first wall. The distribution of remaining tritium in the divertor region were compared with the first orbit loss points calculation of tritons by the LORBIT code. The calculated loss distribution well expressed the measured remaining tritium distribution at the inboard side of the LHD-VV, while the LORBIT calculation overestimated the measured tritium distribution in the region between 45 and 112 degrees in poloidal angle. The difference might come from the effect of collision of EPs with background plasmas, which was not considered in the LORBIT-code. The remaining tritium in the LHD-VV was evaluated to be $\sim 31\%$ of the tritium produced by D–D reaction. This corresponded to about the half of the remaining tritium evaluated from exhaust gas analysis. Further analysis is necessary for an accurate investigation.

Acknowledgments

The author wishes to thank the strong support from the LHD operation team and for their continuous efforts to maintain the safe and steady operation of the LHD. The author also thanks to the former director general of National Institute for Fusion Science, Dr. Yasuhiko Takeiri, for his continuous encouragement to proceed the deuterium experiment at the LHD. This work is partly supported by the NINS program of Promoting Research by Networking among Institutions (Grant Nos. KEIN1601, KEIN1602, KEIN1603, KEIN1604, KEIN1605, KEIN1606 and KEIN1607). The LHD data can be accessed from the LHD data repository at https://www-lhd.nifs.ac.jp/pub/Repository_en.html.

Appendix List of acronyms and their full spells used in this paper

CCW	Counter clock-wise
CW	Clock-wise
CXS	Charge exchange spectroscopy
D–D	Deuterium–deuterium
D–T	Deuterium–tritium
ECH	Electron cyclotron heating

EDS	Exhaust detritiation system
ETB	Edge transport barrier
ETG	Electron temperature gradient mode
FIR	Far infrared
FWP	First wall panel
ILW	ITER like wall
ITB	Internal transport barrier
ITG	Ion temperature gradient mode
LHD	Large helical device
LORBIT	Lorentz ORBIT calculation code
NBI	Neutral beam injector/injection
N-NBI	Negative-ion based NBI
PCA	Primary component analysis
PFC	Plasma facing component
PSL	Photo-stimulated luminescence
RMP	Resonant magnetic-field perturbation
RIC	Resistive interchange mode
TEM	Trapped electron mode
TIPT	Tritium imaging plate technique
VV	Vacuum vessel

ORCID iDs

Masaki Osakabe  <https://orcid.org/0000-0001-5220-947X>
 Hiromi Takahashi  <https://orcid.org/0000-0001-6984-9174>
 Hiroshi Yamada  <https://orcid.org/0000-0003-4546-3167>
 Kenji Tanaka  <https://orcid.org/0000-0002-1606-3204>
 Tatsuya Kobayashi  <https://orcid.org/0000-0001-5669-1937>
 Katsumi Ida  <https://orcid.org/0000-0002-0585-4561>
 Satoshi Ohdachi  <https://orcid.org/0000-0003-2880-9859>
 Jacobo Varela  <https://orcid.org/0000-0002-6114-0539>
 Kunihiro Ogawa  <https://orcid.org/0000-0003-4555-1837>
 Masahiro Kobayashi  <https://orcid.org/0000-0002-0990-7093>
 Katsuyoshi Tsumori  <https://orcid.org/0000-0002-1181-1146>
 Katsunori Ikeda  <https://orcid.org/0000-0001-9781-231X>
 Suguru Masuzaki  <https://orcid.org/0000-0003-0161-0938>
 Masahiro Tanaka  <https://orcid.org/0000-0001-9941-1958>
 Motoki Nakata  <https://orcid.org/0000-0003-2693-4859>
 Sadayoshi Murakami  <https://orcid.org/0000-0002-2526-7137>
 Shigeru Inagaki  <https://orcid.org/0000-0002-4808-857X>
 Kiyofumi Mukai  <https://orcid.org/0000-0003-1586-1084>
 Kazunobu Nagasaki  <https://orcid.org/0000-0001-6423-1754>
 Yasuhiro Suzuki  <https://orcid.org/0000-0001-7618-6305>
 Mitsutaka Isobe  <https://orcid.org/0000-0002-3572-1882>
 Tomohiro Morisaki  <https://orcid.org/0000-0002-4428-5699>

References

- [1] Takeiri Y. 2018 The large helical device: entering deuterium experiment phase toward steady-state helical fusion reactor based on achievements in hydrogen experiment phase *IEEE Trans. Plasma Sci.* **46** 2348

- [2] Osakabe M., Isobe M., Tanaka M., Motojima G., Tsumori K., Yokoyama M., Morisaki T. and Takeiri Y. 2018 Preparation and commissioning for the LHD deuterium experiment *IEEE Trans. Plasma Sci.* **46** 2324
- [3] Takahashi H. et al 2018 Realization of high T_i plasmas and confinement characteristics of ITB plasmas in the LHD deuterium experiments *Nucl. Fusion* **58** 106028
- [4] Nakata M., Nunami M., Sugama H. and Watanabe T.-H. 2016 Impact of hydrogen isotope species on microinstabilities in helical plasmas *Plasma Phys. Control. Fusion* **58** 074008
- [5] Takahashi H. et al 2017 Extension of operational regime in high-temperature plasmas and effect of ECRH on ion thermal transport in the LHD *Nucl. Fusion* **57** 086029
- [6] Yamada H. et al (LHD Experiment Group) 2019 Isotope effect on energy confinement and thermal transport in neutral-beam-heated stellarator-heliotron plasmas *Phys. Rev. Lett.* **123** 185001
- [7] Kobayashi T., Takahashi H., Nagaoka K., Sasaki M., Yokoyama M., Seki R., Yoshinuma M. and Ida K. 2019 Definition of the profile gain factor and its application for internal transport barrier analysis in torus plasmas *Plasma Phys. Control. Fusion* **61** 085005
- [8] Ida K. et al 2019 Measurements of radial profile of hydrogen and deuterium density in isotope mixture plasmas using bulk charge exchange spectroscopy *Rev. Sci. Instrum.* **90** 093503
- [9] Ogawa K. et al 2019 Energetic ion confinement studies using comprehensive neutron diagnostics in the large helical device *Nucl. Fusion* **59** 076017
- [10] Nuga H. et al 2021 Analysis of NB fast-ion loss mechanisms in MHD quiescent LHD plasmas *Plasma Fusion Res.* **16** 2402052
- [11] Ogawa K. et al 2021 A study of beam ion and deuterium–deuterium fusion-born triton transports due to energetic particle-driven magnetohydrodynamic instability in the large helical device deuterium plasmas *Nucl. Fusion* **61** 096035
- [12] Ohdachi S. 2020 Suppression of the energetic particle driven interchange mode in the large helical device *28th IAEA Fusion Energy Con. (FEC 2020)* (Nice 10 – 15 May 2021) (<https://iaea.org/events/fec-2020>)
- [13] Ogawa K. et al 2020 Energetic particle transport and loss induced by helically-trapped energetic-ion-driven resistive interchange modes in the large helical device *Nucl. Fusion* **60** 112011
- [14] Kobayashi M. et al 2013 Control of 3D edge radiation structure with resonant magnetic perturbation fields applied to the stochastic layer and stabilization of radiative divertor plasma in LHD *Nucl. Fusion* **53** 093032
- [15] Kobayashi M. et al 2019 Impact of a resonant magnetic perturbation field on impurity radiation, divertor footprint, and core plasma transport in attached and detached plasmas in the large helical device *Nucl. Fusion* **59** 096009
- [16] Kobayashi M. et al 2021 Confinement improvement during detached phase with RMP application in deuterium plasmas of LHD *Nucl. Fusion* (in press) (<https://doi.org/10.1088/1741-4326/ac42f3>)
- [17] Takahashi H. et al 2020 Performance integration of high temperature plasmas in the LHD deuterium operation *28th IAEA Fusion Energy Con. (FEC 2020)* (Nice 10 – 15 May 2021) (<https://iaea.org/events/fec-2020>)
- [18] Du X.D. et al 2017 Suppression of trapped energetic ions driven resistive interchange modes with electron cyclotron heating in a helical plasma *Phys. Rev. Lett.* **118** 125001
- [19] Varela J., Ohdachi S., Watanabe K.Y., Spong D.A., Garcia L. and Seki R. 2020 Theoretical analysis of energetic-ion-driven resistive interchange mode stabilization strategies using a Landau closure model *Nucl. Fusion* **60** 046013
- [20] Suzuki C., Ida K., Suzuki Y., Yoshida M., Emoto M. and Yokoyama M. 2013 Development and application of real-time magnetic coordinate mapping system in the large helical device *Plasma Phys. Control. Fusion* **55** 014016
- [21] Du X.D. et al 2016 Resistive interchange mode destabilized by helically trapped energetic ions and its effects on energetic ions and bulk plasma in a helical plasma *Nucl. Fusion* **56** 016002
- [22] Tanaka K. et al 2021 Isotope effects on transport in LHD *Plasma Phys. Control. Fusion* **63** 094001
- [23] Yamada H. et al 2020 Investigation of isotope effect on energy confinement time and thermal transport in L-mode plasmas on LHD *28th IAEA Fusion Energy Con. (FEC 2020)* (Nice 10 – 15 May 2021) (<https://iaea.org/events/fec-2020>)
- [24] Cordy J.G. et al 2000 Isotope identity experiments in JET *Plasma Phys. Control. Fusion* **42** A127
- [25] Maggi C.F. et al 2019 Isotope identity experiments in JET-ILW with H and D L-mode plasmas *Nucl. Fusion* **59** 076028
- [26] Kaneko O., Takeiri Y., Tsumori K., Osakabe M., Ikeda K., Nagaoka K. and Nakano H. 2010 Plasma initiation by neutral beam injection *Fusion Sci. Technol.* **58** 497
- [27] Cordy J. G. et al 1999 Plasma confinement in JET H mode plasmas with H, D, DT and T isotopes *Nucl. Fusion* **39** 301
- [28] Luce T.C., Petty C.C. and Cordey J.G. 2008 Application of dimensionless parameter scaling techniques to the design and interpretation of magnetic fusion experiments *Plasma Phys. Control. Fusion* **50** 043001
- [29] Kaye S.M. et al 1997 ITER L-mode confinement database *Nucl. Fusion* **37** 1303
- [30] ITER Physics Expert Group on Confinement Transport, ITER Physics Expert Group on Confinement Database, ITER Physics Basis Editors 1999 Chapter 2: plasma confinement and transport *Nucl. Fusion* **39** 2175
- [31] Tanaka K., Michael C.A., Vyacheslavov L.N., Sanin A.L., Kawahata K., Akiyama T., Tokuzawa T. and Okajima S. 2008 Two-dimensional phase contrast imaging for local turbulence measurements in large helical device (invited) *Rev. Sci. Instrum.* **79** 10E702
- [32] Akiyama T. et al 2010 Interferometer systems on LHD *Fusion Sci. Technol.* **58** 352
- [33] Kobayashi T., Takahashi H., Nagaoka K., Sasaki M., Nakata M., Yokoyama M., Seki R., Yoshinuma M. and Ida K. 2019 Isotope effects in self-organization of internal transport barrier and concomitant edge confinement degradation in steady-state LHD plasmas *Sci. Rep.* **9** 15913
- [34] Kobayashi T. et al 2021 Characterization of isotope effect on ion internal transport barrier and its parameter dependence in large helical device *Nucl. Fusion* **61** 126013
- [35] Murakami S. et al 2004 Effect of neoclassical transport optimization on energetic ion confinement in LHD *Fusion Sci. Technol.* **46** 241
- [36] Osakabe M. et al 2014 Impact of carbon impurities on the confinement of high-ion-temperature discharges in the large helical device *Plasma Phys. Control. Fusion* **56** 095011
- [37] Mukai K. et al 2018 Carbon impurities behavior and its impact on ion thermal confinement in high-ion-temperature deuterium discharges on the large helical device *Plasma Phys. Control. Fusion* **60** 074005
- [38] Ida K. et al 2019 The isotope effect on impurities and bulk ion particle transport in the large helical device *Nucl. Fusion* **59** 056029
- [39] Tokar M.Z., Jaspers R., Weynants R.R., Koslowski H.R., Krämer-Flecken A., Messiaen A.M., Ongena J. and Unterberg B. 1999 Evidence of suppression of ITG-instability in the radiatively improved mode in TEXTOR-94 *Plasma Phys. Control. Fusion* **41** L9
- [40] Tokar M.Z., Ongena J., Unterberg B. and Weynants R.R. 2000 Model for the transition to the radiatively improved mode in a tokamak *Phys. Rev. Lett.* **84** 895
- [41] Bourdelle C., Camenen Y., Citrin J., Marin M., Casson F.J., Koechl F. and Maslov M. 2018 Fast H isotope and impurity

- mixing in ion-temperature-gradient turbulence *Nucl. Fusion* **58** 076028
- [42] Ida K., Yoshinuma M., Tanaka K., Nakata M., Kobayashi T., Fujiwara Y., Sakamoto R., Motojima G. and Masuzaki S. 2021 Characteristics of plasma parameters and turbulence in the isotope-mixing and the non-mixing states in hydrogen-deuterium mixture plasmas in the large helical device *Nucl. Fusion* **61** 016012
- [43] Zong W.L. et al 2016 Experimental observation of turbulence transition and a critical gradient threshold for trapped electron mode in tokamak plasmas *Phys. Plasmas* **23** 060702
- [44] Lee W., Kwon J.M., Ko S.H., Leem J., Yun G.S., Park H.K., Park Y.S., Kim K.W. and Luhmann N.C. 2018 Observation of electron driven quasi-coherent modes and their connection with core intrinsic rotation in KSTAR ECH and ohmic L-mode plasmas *Phys. Plasmas* **25** 022513
- [45] Rice J.E. et al 2011 Rotation reversal bifurcation and energy confinement saturation in tokamak ohmic L-mode plasmas *Phys. Rev. Lett.* **107** 265001
- [46] Ida K. et al 2020 Transition between isotope-mixing and non-mixing state in hydrogen-deuterium mixture plasmas *Phys. Rev. Lett.* **124** 025002
- [47] Varela J., Spong D.A., Garcia L., Ohdachi S., Watanabe K.Y. and Seki R. 2019 Analysis of the MHD stability and energetic particles effects on EIC events in LHD plasma using a Landau-closure model *Nucl. Fusion* **59** 046008
- [48] Yamada H., Watanabe K.Y., Sakakibara S., Suzuki Y., Ohdachi S., Kobayashi M. and Funaba H. (LHD Experiment Group) 2010 Study of high-beta plasmas in a helical system *Contrib. Plasma Phys.* **50** 480
- [49] Heidbrink W.W., Duong H.H., Manson J., Wilfrid E., Oberman C. and Strait E.J. 1993 The nonlinear saturation of beam-driven instabilities: theory and experiment *Phys. Fluids B* **5** 2176
- [50] Sudo S., Takeiri Y., Zushi H., Sano F., Itoh K., Kondo K. and Iiyoshi A. 1990 Scalings of energy confinement and density limit in stellarator/heliotron devices *Nucl. Fusion* **30** 11
- [51] Evans T.E. 2105 Resonant magnetic perturbations of edge-plasmas in toroidal confinement devices *Plasma Phys. Control. Fusion* **58** 123001
- [52] Kobayashi M. and Tokar M.Z. 2020 Time-dependent plasma transport simulation for the study of edge impurity radiation dynamics with magnetic island in large helical device *Contrib. Plasma Phys.* **60** e201900138
- [53] Takeiri Y. et al 2010 High performance of neutral beam injectors for extension of LHD operational regime *Fusion Sci. Technol.* **58** 482
- [54] Tsumori K. et al 2010 Research and development activities on negative ion sources *Fusion Sci. Technol.* **58** 482
- [55] Tsumori K. et al 2010 Beamlet characteristics in the accelerator with multi-slot grounded grid *Rev. Sci. Instrum.* **58** 482
- [56] Ikeda K., Tsumori K., Nakano H., Kasaki M., Nagaoka K., Kamio S., Fujiwara Y., Haba Y. and Osakabe M. 2019 Exploring deuterium beam operation and the behavior of the co-extracted electron current in a negative-ion-based neutral beam injector *Nucl. Fusion* **59** 076009
- [57] Tsumori K. et al 2021 Challenge toward improvement of deuterium injection power in LHD negative-ion-based NBIs *Nucl. Fusion* (<https://doi.org/10.1088/1741-4326/ac2d59>)
- [58] Masaki K., Yagyu J., Arai T., Kaminaga A., Kodama K., Miya N., Ando T., Hiratsuka H. and Saidoh M. 2002 Wall conditioning and experience of the carbon-based first wall in JT-60U *Fusion Sci. Technol.* **42** 386
- [59] Sartori R., Saibene G., Goodall D.H.J., Usselmann E., Coad P. and Holland D. 1990 Deuterium release measurements in the Be phase of JET and determination of tritium content in the exhaust gas *J. Nucl. Mater.* **176–177** 624
- [60] Usselmann E., Hemmerich J.L., Holland D., Grobusch L., Schargitz U., Sartori R. and Saibene G. 1990 Experimental set-up for gas balance measurement at JET *Vacuum* **41** 1515
- [61] Sugiyama K. et al 2004 Tritium profile in plasma-facing components following D–D operation *J. Nucl. Mater.* **329–333** 874
- [62] Tanaka M., Suzuki N. and Kato H. 2020 Exhaust behavior of tritium from the large helical device in the first deuterium plasma experiment *J. Nucl. Sci. Technol.* **57** 1297
- [63] Tanaka M., Kato H., Suzuki N., Masuzaki S., Yajima M., Nakada M. and Iwata C. 2020 Tritium balance in large helical device during and after the first deuterium plasma experiment campaign *Plasma Fusion Res.* **15** 1405062
- [64] Isobe M. et al 2018 Neutron diagnostics in the large helical device *IEEE Trans. Plasma Sci.* **46** 2050
- [65] Nakano Y., Yamazaki A., Watanabe K., Uritani A., Ogawa K. and Isobe M. 2014 Study on *in situ* calibration for neutron flux monitor in the large helical device based on Monte Carlo calculations *Rev. Sci. Instrum.* **85** 11E116
- [66] Nishitani T. et al 2016 Calibration experiment and the neutronics analyses on the LHD neutron flux monitors for the deuterium plasma experiment *Fus. Eng. Des.* **136** 210
- [67] Masuzaki S. et al 2020 Investigation of remaining tritium in the LHD vacuum vessel after the first deuterium experimental campaign *Phys. Scr.* **T171** 014068
- [68] Masuzaki S., Yajima M., Ogawa K., Motojima G., Tanaka M., Tokitani M., Isobe M. and Otsuka T. 2021 Investigation of the distribution of remaining tritium in divertor in LHD *Nucl. Mater. Energy* **26** 100884
- [69] Yajima M., Masuzaki S., Yoshida N., Tokitani M., Otsuka T., Oya Y., Torikai Y. and Motojima G. 2021 Investigation on tritium retention and surface properties on the first wall in the large helical device *Nucl. Mater. Energy* **27** 100906
- [70] Masuzaki S. et al 2020 Distribution of remaining tritium in the LHD vacuum vessel 28th IAEA Fusion Energy Con. (FEC 2020) (Nice 10 – 15 May 2021) (<https://iaea.org/events/fec-2020>)
- [71] Ogawa K., Isobe M., Nishitani T., Murakami S., Seki R., Nuga H., Pu N. and Osakabe M. 2019 Study of first orbit losses of 1 MeV tritons using the Lorentz orbit code in the LHD *Plasma Sci. Technol.* **21** 025102